

MOJAVE: XVIII. Kinematics and Inner Jet Evolution of Bright Radio-Loud Active Galaxies

M. L. LISTER,¹ D. C. HOMAN,² K. I. KELLERMANN,³ Y. Y. KOVALEV,^{4,5,6} A. B. PUSHKAREV,^{7,4,5} E. ROS,⁶ AND
T. SAVOLAINEN^{8,9,6}

¹*Department of Physics and Astronomy, Purdue University, 525 Northwestern Avenue, West Lafayette, IN 47907, USA*

²*Department of Physics, Denison University, Granville, OH 43023, USA*

³*National Radio Astronomy Observatory, 520 Edgemont Road, Charlottesville, VA 22903, USA*

⁴*Astro Space Center of Lebedev Physical Institute, Profsoyuznaya 84/32, 117997 Moscow, Russia*

⁵*Moscow Institute of Physics and Technology, Institutskiy per. 9, Dolgoprudny, Moscow region, 141700, Russia*

⁶*Max-Planck-Institut für Radioastronomie, Auf dem Hügel 69, 53121 Bonn, Germany*

⁷*Crimean Astrophysical Observatory, 98409 Nauchny, Crimea, Russia*

⁸*Aalto University Department of Electronics and Nanoengineering, PL 15500, FI-00076 Aalto, Finland*

⁹*Aalto University Metsähovi Radio Observatory, Metsähovintie 114, FI-02540 Kylmälä, Finland*

(Received 2021 July 19; Revised 2021 August 23; Accepted 2021 August 27)

Submitted to *Astrophysical Journal*

ABSTRACT

We have analyzed the parsec-scale jet kinematics of 447 bright radio-loud AGN, based on 15 GHz VLBA data obtained between 1994 August 31 and 2019 August 4. We present new total intensity and linear polarization maps obtained between 2017 January 1 to 2019 August 4 for 143 of these AGN. We tracked 1923 bright features for five or more epochs in 419 jets. A majority (60%) of the well-sampled jet features show either accelerated or non-radial motion. In 47 jets there is at least one non-accelerating feature with an unusually slow apparent speed. Most of the jets show variations of 10° to 50° in their inner jet position angle (PA) over time, although the overall distribution has a continuous tail out to 200°. AGN with SEDs peaked at lower frequencies tend to have more variable PAs, with BL Lacs being less variable than quasars. The *Fermi* LAT gamma-ray associated AGN also tend to have more variable PAs than the non-LAT AGN in our sample. We attribute these trends to smaller viewing angles for the lower spectral peaked and LAT-associated jets. We identified 13 AGN where multiple features emerge over decade-long periods at systematically increasing or decreasing PAs. Since the ejected features do not fill the entire jet cross-section, this behavior is indicative of a precessing flow instability near the jet base. Although some jets show indications of oscillatory PA evolution, we claim no bona fide cases of periodicity since the fitted periods are comparable to the total VLBA time coverage.

Keywords: Active galactic nuclei (16), BL Lacertae objects (158), Gamma-ray sources (633), Radio galaxies (1343), Radio jets (1347), Quasars (1319)

1. INTRODUCTION

Relativistic jets from active galactic nuclei (AGN) represent some of the most energetic long term phenomena in the universe, and played a key role in regulating galaxy formation via feedback processes (e.g., Fabian 2012). A powerful tool for investigating these outflows is the Very Long Baseline Array (VLBA), which provides full polarization, sub-milliarcsecond scale imaging at radio wavelengths. The latter has revealed important details of the pc-scale structural and magnetic field

evolution of AGN jets (Blandford et al. 2019; Wardle 2013), and is a critical driver for state of the art numerical jet simulations (Davis & Tchekhovskoy 2020; Komissarov & Porth 2021).

Since the VLBA's commissioning in 1994, we have carried out a program to investigate the parsec-scale properties of several hundred of the brightest AGN jets in the northern sky above J2000 declination -30° . This effort started out as the 2 cm VLBA survey (Kellermann et al. 1998), and continued as the MOJAVE survey in 2002

with the addition of full polarization imaging of a complete flux density-limited sample (Lister & Homan 2005). We have presented our findings in a number of papers in this series, including our most recent analysis of jet kinematics based on multi-epoch data obtained between 1994 August 31 and 2016 December 26 (Lister et al. 2019).

In this paper we perform a new kinematics analysis that adds VLBA data taken up to and including 2019 August 4, and increases the number of AGN jets in our study from 409 to 447. Some of these jets have no new data after the cutoff date of our previous kinematics paper (Lister et al. 2019), but we have made some revisions to their model fits. For this reason we tabulate here the fit values for all 447 jets, which supersede those presented in previous papers. We have excluded several AGN that were in the Lister et al. (2019) analysis since we subsequently determined that they have uncertain core locations and less reliable kinematic fits. These consist of NGC 1052, which has a heavily absorbed core at 15 GHz (Vermeulen et al. 2003), five compact symmetric objects (B2 0026+34, S4 0108+38, S4 0646+60, B3 0710+439, and TXS 2021+614), and five AGN with extremely compact radio structure that appear unresolved or barely resolved (PKS 0414–189, S5 0615+82, TXS 0640+090, TXS 1739+522, and B2 2023+33). We will present a kinematic analysis of the compact symmetric object jets in a future paper in this series.

The size and time coverage of our data set provides a unique opportunity to examine the stability of the innermost regions of AGN jets over time. Although smoking gun evidence of AGN jet precession has been seen on kpc-scales (e.g., Smith & Donohoe 2019; Falceta-Gonçalves et al. 2010; Gower et al. 1982), there have been few large systematic pc-scale studies to date. In Lister et al. (2013) we identified several individual cases of AGN that may be undergoing periodic changes in their inner jet position angle (PA). We revisit our earlier study by analyzing a much larger data set consisting of 173 jets that have 12 or more VLBA observations acquired over a minimum 10 year period. We provide evidence that over time, AGN eject narrow jet features at different position angles within a broader outflow, resulting in apparent changes in their inner jet direction on the sky. The range and variance of these changes is larger for jets oriented closer to the line of sight. In some AGN jets the PAs of successively ejected features follow a systematic trend over time, indicating a wobbling flow instability near the jet base from which the features emerge. Occasionally this instability may be disrupted and/or a new instability forms at another location, resulting in a sudden jump in the inner jet PA.

The layout of our paper is as follows. In Section 2 we describe our VLBA data and reduction methods, as well as the general properties of our AGN jet sample. We describe our kinematics analysis method in Section 3, and present our study of inner jet position angle variations. We summarize our findings in Section 4. Throughout this paper we use the cosmological parameters $\Omega_m = 0.27$, $\Omega_\Lambda = 0.73$ and $H_o = 71 \text{ km s}^{-1} \text{ Mpc}^{-1}$ (Komatsu et al. 2009) and define sky position angles in degrees east of north.

2. OBSERVATIONAL DATA

2.1. MOJAVE Data Archive

As of 2021, the MOJAVE data archive¹ consists of nearly ten thousand 15 GHz (2 cm) VLBA observations of over 500 AGN dating back to 1994, obtained as part of the 2 cm VLBA survey (Kellermann et al. 1998), the NRAO archive,² and the MOJAVE program. The MOJAVE data archive provides public access to calibrated visibility and image FITS files for these observations. Over time, we have added AGN on the basis of their correlated flux density, high-energy gamma-ray emission, or membership in other AGN monitoring programs. The minimum criteria are a J2000 declination $> -30^\circ$ to ensure sufficient interferometric visibility plane coverage, and a 15 GHz VLBA flux density larger than $\sim 50 \text{ mJy}$ to ensure direct fringe detection and the ability to self-calibrate the data.

In Lister et al. (2019), we compiled a complete flux density limited AGN sample, the 1.5 Jy Quarter Century MOJAVE sample (1.5JyQC), consisting of all 232 AGN north of J2000 declination -30° known to have exceeded 1.5 Jy in 15 GHz VLBA flux density at any time between 1994.0 and 2019.0. This is the largest and most complete radio-loud blazar sample to date, covering 75% of the entire sky. Being a multi-epoch sample selected only on the basis of parsec-scale jet emission, it is well-suited for investigating the effects of relativistic beaming on observed blazar luminosity functions (Cara & Lister 2008), and the properties of the misaligned (parent) population (Lister et al. 2019).

In Lister & Homan (2005); Lister et al. (2009a, 2013, 2018), we have published 15 GHz total intensity and linear polarization maps from the MOJAVE program up to 2016 Dec 26. Here we present new 15 GHz VLBA maps of 143 AGN obtained between 2017 Jan-

¹ <http://www.physics.purdue.edu/MOJAVE>

² <http://archive.nrao.edu>

Table 1. MOJAVE AGN Properties

B1950	Alias	Opt.	z	Optical Reference	LAT Association	TeV	1.5 Jy	ν_{pk}	Ref.
(1)	(2)	(3)	(4)	(5)	(6)	(7)	(8)	(9)	(10)
0003+380	S4 0003+38	Q	0.229	Schramm et al. (1994)	4FGL J0005.9+3824	13.1	10
0003-066	NRAO 005	B	0.347	Jones et al. (2005)	4FGL J0006.3-0620	...	Y	12.9	9
0006+061	TXS 0006+061	B	...	Rau et al. (2012)	4FGL J0009.1+0628	13.4	10
0007+106	III Zw 2	G	0.089	Sargent (1970)	^a	...	Y	13.3	1
0011+189	RGB J0013+191	B	0.477	Shaw et al. (2013)	4FGL J0014.1+1910	13.7	9
0010+405	4C +40.01	Q	0.256	Thompson et al. (1992)	4FGL J0013.6+4051	12.8	9
0012+610	4C +60.01	U	4FGL J0014.8+6118	13.1	10
0014+813	S5 0014+813	Q	3.382	Varshalovich et al. (1987)	12.5	1
0015-054	PMN J0017-0512	Q	0.226	Shaw et al. (2012)	4FGL J0017.5-0514	13.6	10
0016+731	S5 0016+73	Q	1.781	Lawrence et al. (1986)	4FGL J0019.6+7327	...	Y	12.3	9
0019+058	PKS 0019+058	B	...	Truebenbach & Darling (2017)	4FGL J0022.5+0608	13.1	10

NOTE—Columns are as follows: (1) B1950 name, (2) other name, (3) optical spectroscopic classification, where B = BL Lac, Q = quasar, G = radio galaxy, N = narrow-line Seyfert 1, and U = unknown, (4) redshift, (5) reference for redshift and/or optical classification. (6) high confidence GeV gamma-ray association from Fermi LAT catalogs, where 4FGL = Abdollahi et al. (2020); Ballet et al. (2020), 3FGL = Acero et al. (2015), 2FGL = Nolan et al. (2012), 1FGL = Abdo et al. (2010). (7) known TeV gamma-ray emitter (<http://tevcat.uchicago.edu>). (8) member of the VLBA 15 GHz flux density-limited 1.5 Jy Quarter Century Sample (Lister et al. 2019). (9) log frequency of synchrotron peak in spectral energy distribution in Hz. (10) reference for synchrotron peak frequency, where 1. ASDC SED builder (Stratta et al. 2011) 2. Meyer et al. (2011) 3. Nieppola et al. (2008) 4. Ackermann et al. (2011) 5. Nieppola et al. (2006) 6. Abdo et al. (2009a) 7. Abdo et al. (2009b) 8. Hervet et al. (2015) 9. Ajello et al. (2020) 10. Ackermann et al. (2015) 11. Xiong et al. (2015) 12. Chang et al. (2017) 13. Ajello et al. (2017) 14. Chang et al. (2019)

This table is published in its entirety in the machine-readable format. A portion is shown here for guidance regarding its form and content.

^a Fermi-LAT detection reported by Arsioli & Polenta (2018)

^b Fermi-LAT detection announced in <https://www.astronomerstelegam.org/?read=14383>.

uary 3 and 2019 August 4. The 49 new AGN included here are members of either the Robopol optical polarization survey (Blinov et al. 2021), the *Fermi* 2FHL catalog (Ackermann et al. 2016), the LAT monitored list of flaring sources³, or the MOJAVE-*Fermi* hard spectrum gamma-ray sample (Lister et al. 2018). We list the general properties of all the MOJAVE AGN in Table 1. We have compiled synchrotron peak frequencies from the literature, or used the fit routines provided by the ASDC spectral energy distribution (SED) builder (Stratta et al. 2011). The optical classifications and redshifts are compiled from the NED database, with the literature references listed in column 5 of Table 1. Of the 68 AGN with unknown redshift, 57 are classified as BL Lacs due to their near-featureless optical spectrum in the reference listed in Table 1. Some of the remaining 11 AGN have been classified as BL Lacs by other authors on the basis of their gamma-ray properties, however, we classify these as unknown since they lack published optical spectra. We provide notes on selected individual AGN in the Appendix A.

³ <https://heasarc.gsfc.nasa.gov/W3Browse/fermi/fermilasp.html>

2.2. Data Reduction

We processed the VLBA data using standard reduction methods in AIPS (Greisen 2003), and self-calibrated and imaged the visibilities in DIFMAP (Shepherd 1997). We determined the absolute EVPA correction at each epoch via measurements of stable downstream polarized features, as described in our previous papers (Lister et al. 2018, 2019). The EVPAs were originally anchored using near-simultaneous single dish polarization measurements at 15 GHz made at the U. Michigan Radio Observatory (Aller et al. 2003).

While comparing our total cleaned VLBA flux densities (S_{VLBA}) to near-simultaneous single-dish 15 GHz observations made by the Owens Valley 40m radio monitoring program (S_{OVRO} ; Richards et al. 2011), we discovered a persistent error affecting the VLBA visibility amplitudes. All VLBA data obtained after 2019 April 15 have suffered from a systematic $\sim 15\% - 25\%$ decrease in correlated flux density on all baselines. At the time of writing the cause of this drop is unknown and is being investigated. We applied flux density correction factors to all the visibilities in four affected VLBA epochs listed in subsection 2. We determined these corrections by first estimating the amount of arcsecond-scale flux density resolved out by the VLBA (S_{res}) for

Table 2. VLBA Flux Density Correction Factors

Epoch	Obs. Code	Correction Factor
2019 June 13	BL229AX	1.18
2019 June 29	BL229AY	1.15
2019 July 19	BL229AZ	1.27
2019 August 4	BL273A	1.26

individual MOJAVE AGN based on multiple previous near-simultaneous OVRO–VLBA measurements dating back to 2008. These were typically $\lesssim 5\%$ of the OVRO flux density, reflecting the highly core-dominated nature of the MOJAVE sample AGN. At each VLBA epoch, we determined a correction factor for each AGN $c = (S_{\text{OVRO}} - S_{\text{res}})/S_{\text{VLBA}}$ and computed the median of these values.

2.3. VLBA 15 GHz Maps

In Figure Set 1 we present 648 maps of 142 AGN spanning epochs from 2017 January 1 to 2019 August 4. To supplement our kinematics analysis we processed two data sets (3C 264 and IVS B1147+245; epoch 2018 March 30, VLBA observation code BM482) from the VLBA archive, and one from Lister et al. (2020) (TXS 0128+554 epoch 2018 June 29, VLBA observation code BL251). The remaining data come from the MOJAVE program (VLBA observation codes BL229 and BL273).

Since any absolute sky positional information is lost during the self-calibration process, we shifted the origin of each map to the total intensity Gaussian model-fit position of the core feature, as described in § 3.1. The core is typically the brightest feature in the map, located at the optically thick surface close to the base of the jet.

In each ‘dual-plot’ map in Figure Set 1, we indicate the FWHM dimensions and orientation of the naturally-weighted elliptical Gaussian restoring beam by a cross in the lower left corner. The beam size varies with the declination of the AGN and number of available antennas, but has typical dimensions of $1.1 \text{ mas} \times 0.5 \text{ mas}$. We gridded the Stokes maps with a scale of 0.1 mas per pixel. We list the parameters of the restoring beam, base contour levels, total cleaned flux densities, and blank sky map noise levels for each map in Table 3. The false color corresponds to fractional polarization, and is superimposed on a total intensity contour map of the radio emission. No fractional polarization is plotted in regions that lie below the lowest total intensity contour level. The latter typically corresponds to roughly 3 times the rms noise level of the map, although this can be higher in the

cases of AGN with poorer interferometric coverage due to extreme southern or near-equatorial declination, or very bright jet cores due to dynamic range limitations.

We plot a second map of the source, in blue linear polarization contours increasing by successive factors of two, at an arbitrary sky position offset from the total intensity map, along with a single lowest total intensity contour in grey. The overlaid sticks indicate the observed electric vector directions, and are of arbitrary fixed length. We have not corrected their orientations for any Faraday rotation either internal or external to the AGN jet. Our rotation measure study of the MOJAVE sample (Hovatta et al. 2012) showed that the emission from most of these jets experiences only a few degrees of Faraday rotation at 15 GHz, typically in the region near the base of the jet. The lowest polarization contour is typically 3 times $\sigma_{\text{Q,U}}$, but in $\sim 14\%$ of the epochs is more than 5 times $\sigma_{\text{Q,U}}$ due to a high peak total intensity in the map, or residual polarization feed leakage errors. We have not applied any Rician debiasing corrections (i.e., $P_{\text{corr}} = P_{\text{obs}} \sqrt{1 - (\sigma_P/P_{\text{obs}}^2)}$; Wardle & Kronberg 1974) to the maps, since these are $\lesssim 5\%$ for regions above our lowest polarization contour level.

3. DATA ANALYSIS

For our kinematics analysis we have used 15.4 GHz VLBA observations of 447 AGN obtained between 1994 August 31 and 2019 August 4 as part of the MOJAVE and 2 cm VLBA survey programs, with supplementary data from the NRAO archive. There are 49 AGN which have not appeared previously in any MOJAVE kinematics analysis. Although the density and span of time coverage varies considerably among the sample, all of the AGN in the kinematics analysis have at least 5 high quality VLBA epochs over a 1.5 year to 25 year time span.

3.1. Gaussian Modeling

We modeled the sky brightness distribution for each VLBA observation in the (u, v) visibility plane using the *modelfit* task in DIFMAP. We list the properties of the fitted features in Table 4. In some instances, it was impossible to robustly cross-identify the same features in a jet from one epoch to the next. We indicate the features with robust cross-identifications across at least five epochs in column 10 of Table 4. In making robustness determinations, we considered the consistency of evolution in the sky position, flux density, and brightness temperature of the features over time. For the non-robust

Table 3. 15 GHz Map Parameters

Source	Epoch	B_{maj}	B_{min}	B_{pa}	I_{tot}	σ_{I}	I_{base}	P_{tot}	$\sigma_{\text{Q,U}}$	P_{base}	EVPA	Fig.
(1)	(2)	(3)	(4)	(5)	(6)	(7)	(8)	(9)	(10)	(11)	(12)	(13)
0012+610	2017 Jan 3	0.80	0.64	-6	257	0.12	0.33	< 0.4	0.13	0.44	...	1.1
	2017 Mar 11	0.73	0.66	0	252	0.09	0.26	2.3	0.10	0.32	159	1.2
	2017 Jun 17	0.66	0.60	-17	232	0.10	0.23	1.6	0.11	0.30	167	1.3
	2017 Aug 25	0.71	0.58	-6	235	0.11	0.25	2.7	0.12	0.35	177	1.4
	2018 May 31	0.68	0.60	-2	247	0.10	0.25	2.4	0.10	0.40	162	1.5
	2019 Jun 29	0.86	0.66	-28	274	0.14	0.35	1.5	0.15	0.46	178	1.6
0014+813	2017 Jan 28	0.71	0.66	70	828	0.10	0.33	10	0.10	0.35	168	1.7
	2017 Jun 17	0.67	0.59	82	853	0.10	0.30	10	0.10	0.35	171	1.8
	2017 Nov 18	0.82	0.72	-52	922	0.11	0.90	7.1	0.13	0.51	171	1.9
	2018 Feb 2	0.72	0.68	23	904	0.11	0.34	11	0.14	0.52	178	1.10
	2018 Jul 8	0.63	0.55	-12	849	0.12	0.35	20	0.12	0.46	175	1.11
	2018 Nov 11	0.67	0.59	42	963	0.13	0.38	27	0.13	0.60	177	1.12
	2019 Jan 19	0.63	0.61	19	957	0.12	0.47	26	0.18	0.65	177	1.13
	2019 Jun 29	0.74	0.71	14	1077	0.14	1.04	27	0.15	0.75	2	1.14

^aNRAO archive epoch

NOTE—Columns are as follows: (1) B1950 name, (2) date of VLBA observation, (3) FWHM major axis of restoring beam (milliarcseconds), (4) FWHM minor axis of restoring beam (milliarcseconds), (5) position angle of major axis of restoring beam (degrees), (6) total cleaned I flux density (mJy), (7) rms noise level of Stokes I image (mJy per beam), (8) lowest I contour level (mJy per beam), (9) total cleaned P flux density (mJy), or upper limit, based on 3 times the P rms noise level, (10) average of blank sky rms noise level in Stokes Q and U images (mJy per beam), (11) lowest linear polarization contour level (mJy per beam), (12) integrated electric vector position angle (degrees), (13) figure number. This table is published in its entirety in the machine-readable format. A portion is shown here for guidance regarding its form and content.

features, we caution that the assignment of the same identification number across epochs does not necessarily indicate a reliable cross-identification. We initially assigned the identification numbers in ascending order roughly based on their distance from the core, but in many cases the original order had to be modified during the cross-identification process.

Based on previous analysis (Lister et al. 2009b), we estimate the typical uncertainties in the feature centroid positions to be $\sim 20\%$ of the FWHM naturally-weighted image restoring beam dimensions. For isolated bright and compact features, the positional errors are smaller by approximately a factor of two. We estimate the formal errors on the feature sizes to be roughly twice the positional error, according to Fomalont (1999). The flux density accuracies are approximately 5% (see Appendix A of Homan et al. 2002), but can be significantly larger for features located very close to one another. Also, at some epochs which lacked data from one or more antennas, the fit errors of some features are much larger. We do not use the latter in our kinematics or jet position angle analyses, and indicate them with flags in Table 4.

3.2. Jet Kinematics

We analyzed the kinematics of all individual robust jet features using three methods: (i) a simple one-dimensional radial motion fit, (ii) a non-accelerating vector fit in two dimensions (right ascension and declination), and (iii) a constant acceleration two-dimensional fit (for features with ten or more epochs). We use the radial fit for diagnostic purposes only, and do not tabulate those fit results here. In all cases, we assume the bright core feature (id 0 in Table 4) to be stationary, and measure the positions of jet features at all epochs with respect to it. We described the details of the fitting method in Lister et al. (2019). We note that flaring activity, a not-yet-resolved newly-ejected feature, or the variable core-shift effect (Plavin et al. 2019) can sometimes result in core positional variations. In cases where a large shift of the core was observed, we flagged that epoch from the kinematics analysis.

We made radial and vector motion fits using all of the available data from 1994 August 31 to 2019 August 4 on 1923 robust jet features in 447 jets. A total of 28 of these jets had no robust features for kinematic analysis due to weak/absent downstream jet flux density, an insufficiently stable core feature, and/or insufficient angular resolution.

In Table 5 we list the results of our vector motion fits. Due to the nature of our kinematic model, which

Table 4. Fitted Jet Features

Source	I.D.	Epoch	I (mJy)	r (mas)	P.A. ($^{\circ}$)	Maj. (mas)	Ratio	Maj. P.A. ($^{\circ}$)	Robust?
(1)	(2)	(3)	(4)	(5)	(6)	(7)	(8)	(9)	(10)
0003+380	0	2006 Mar 9	489	0.04	290.7	0.23	0.33	292	Y
0003+380	1	2006 Mar 9	7.2	3.98	121.8	0.72	1	...	Y
0003+380	2	2006 Mar 9	42.1	1.25	110.5	0.51	1	...	Y
0003+380	6	2006 Mar 9	104	0.28	114.6	0.27	1	...	Y
0003+380	7	2006 Mar 9	2.9	2.31	119.3	N
0003+380	0	2006 Dec 1	320	0.10	308.1	0.25	0.29	295	Y
0003+380	1	2006 Dec 1	4.8	3.65	120.8	1.63	1	...	Y
0003+380	2	2006 Dec 1	20.9	1.56	111.0	0.25	1	...	Y
0003+380	5	2006 Dec 1	22.9	0.75	116.2	0.32	1	...	Y
0003+380	6	2006 Dec 1	145	0.45	116.3	0.05	1	...	Y

^a Individual feature epoch not used in kinematic fits.

NOTE—Columns are as follows: (1) B1950 name, (2) feature identification number (zero indicates core feature), (3) observation epoch, (4) flux density at 15 GHz in mJy, (5) position offset from the core feature (or map center for the core feature entries) in milliarcseconds, (6) position angle with respect to the core feature (or map center for the core feature entries) in degrees, (7) FWHM major axis of fitted Gaussian in milliarcseconds, (8) axial ratio of fitted Gaussian, (9) major axis position angle of fitted Gaussian in degrees, (10) robust feature flag. This table is published in its entirety in the machine-readable format. A portion is shown here for guidance regarding its form and content.

naturally includes the possibility of accelerated motion, we did not estimate ejection epochs (Column 12) for any features where we could not confidently extrapolate their motion to the core. Jet features for which we list an ejection epoch had the following properties: (i) significant motion ($\mu \geq 3\sigma_{\mu}$), (ii) no significant acceleration, (iii) a velocity vector direction ϕ within 15° of the outward radial direction to high confidence, i.e., $|\langle\vartheta\rangle - \phi| + 2\sigma \leq 15^{\circ}$, where ϑ is the mean position angle, (iv) an extrapolated position at the ejection epoch no more than 0.2 mas from the core, and (v) a fitted ejection epoch that differed by no more than 0.5 years from that given by the radial motion fit.

Approximately half ($N = 926$) of the robust features met the ≥ 10 epoch criterion for an acceleration fit, and we tabulate these results in Table 6. The majority (60%) of these well-sampled features display either significant acceleration or non-radial motion.

We have marked 64 features in Table 6, in 47 different AGN, that have appreciably slower speeds than other features in the same jet. These slow pattern speed features (i) do not have a $\geq 3\sigma$ acceleration, (ii) have an angular speed smaller than $20 \mu\text{as y}^{-1}$, and (iii) have a speed at least ten times slower than the fastest feature in the same jet.

We also include flags in Table 5 and 6 for inward-moving features. In Lister et al. (2019) we discuss the possibility that some of these may be the result of centroid shifts in diffuse emission regions, or curved tra-

jectories crossing the line of sight. Of the 1923 robust features in our latest analysis, only 48 show apparent inward motion. Although this fraction (2.5%) is small, 39 of the AGN jets in our sample (8.7%) show this phenomenon. We provide updated information on selected AGN with inward-moving features in Appendix A. In an earlier paper (Lister et al. 2009a) we discussed the five AGN in the original flux density-limited MOJAVE sample that have counter-jet features: 0238–084 (NGC 1052), 0316+413 (3C 84), 1228+126 (M87), PKS 1413+135, and 1957+405 (Cyg A). With the exception of PKS 1413+135, these are all nearby ($z < 0.06$) radio galaxies with jets much closer to the plane of the sky than the other AGN in our sample. PKS 1413+135 is a peculiar AGN with blazar properties that may be a gravitationally lensed system (see Readhead et al. 2021 and references therein). In our current analysis we find only two new examples of candidate counter-jets in the 1.5JyQC sample: 1928+738 and 1253–055 (3C 279), but in both cases we believe that these are not actual counter-jets, and that the true core is visible only at some epochs (see Appendix notes). Among the non-1.5JyQC AGN presented in this paper, there are only a handful with counter-jet features. These consist of two compact symmetric objects TXS 0128+554 and 1509+054 (PMN J1511+0518), two giant radio galaxies 1637+826 (NGC 6251) and 2043+749 (4C +74.26), the nearby ($z = 0.029$) radio galaxy 0305+039 (3C 78), and the quasar 1148–001 (4C –00.47). In the

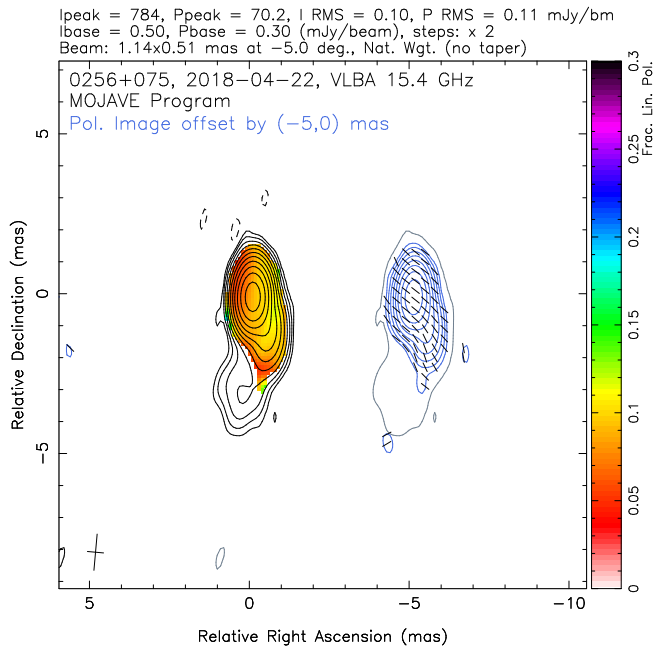


Figure 1. 15 GHz VLBA maps of the MOJAVE AGN sample. Each panel contains two contour maps of the radio source, the first consisting of I contours in successive integer powers of two times the lowest contour level, with linear fractional polarization overlaid according to the color wedge. A single negative I contour equal in magnitude to the base contour level is also plotted with dashed lines. The second map includes the lowest positive I contour from the first map in black, and linearly polarized intensity contours in blue, also increasing by factors of two. The sticks indicate the electric polarization vector directions, uncorrected for Faraday rotation. The FWHM dimensions and orientation of the elliptical Gaussian restoring beam are indicated by a cross in the lower left corner of the map. The parameters of each map are listed in Table 3. (The complete figure set is available in the online journal.)

latter AGN, we have assumed the core to be the most compact feature of the jet, but higher frequency VLBA observations are needed to more precisely determine its location. In Table 4 we also list a counter-jet feature for the high redshift $z = 2.624$ quasar PKS B0742+103, but the core location is uncertain in this source as noted in the Appendix.

In Table 7 we tabulate a median speed for each jet having at least 5 features with $\geq 3\sigma$ speeds; we excluded any counter-jet features, and those flagged as having inward motion. For features with $\geq 3\sigma$ accelerations we

used the speed from the acceleration fit, otherwise we used the vector motion fit speed. The error for the median speed in Table 7 is either that of the middle value in the distribution, or the mean of the two middle values for jets with an even number of speed measurements. We also tabulated a maximum speed for each jet using the same criteria. If a jet had no $\geq 3\sigma$ speed features, we used the fastest $\geq 2\sigma$ speed, or otherwise, the speed with the lowest error value.

In the left hand panels of Figure 2 we plot the distribution of median and maximum apparent jet speeds of all the AGN in our sample with known redshifts. We show the distributions for the 1.5 Jy QC sample AGN in the right hand panels. The maximum speed distribution for the full sample (lower left panel) is peaked below $2c$, but 45% of the jets in the first bin have 2 or fewer robust features. The maximum speed distribution for jets with at least five robust features (lower panel, shaded) is not sharply peaked, suggesting that multiple features must typically be tracked in a jet to get a more robust measure of the overall flow speed. The 1.5 Jy QC sample AGN have typically been tracked in the MOJAVE program for longer time periods, so their maximum speed distribution is not as sharply peaked.

In Figure Set 3 we plot the angular separation of features from the core in each jet versus time. The robust features have filled colored symbols and solid lines representing the fit. The feature identification number is overlined if the acceleration model was fit and yielded a $\geq 3\sigma$ acceleration. An underlined identification number indicates a feature with non-radial motion, i.e., its velocity vector does not point back to the core location within the errors. We plot the individual trajectories and fits on the sky for all the robust features in Figure Set 4.

3.3. Inner Jet Position Angle Analysis

In Lister et al. (2013) we presented the first large survey of inner PA variations in AGN jets based on data from 1994 to 2011, where we found evidence for large changes in jet PA within ~ 1 mas (~ 8 pc projected at $z = 1$) of the core over decadal timescales, in some cases as fast as 10° yr^{-1} . Here we carry out a new analysis, using additional data obtained between 2011 May 21 and 2019 August 4. Our main goals are to: (i) determine the PA of the jet as close as possible to the core feature, using the maximum angular resolution of the VLBA data at 15 GHz, and (ii) examine the behavior of the inner jet PA over time in individual jets and among different AGN classes.

In our previous study we determined the inner jet PA using a flux-density weighted position angle average of

Table 5. Vector Motion Fit Properties of Jet Features

Source	I.D.	N	$\langle S \rangle$ (mJy)	$\langle R \rangle$ (mas)	$\langle d_{\text{proj}} \rangle$ (pc)	$\langle \vartheta \rangle$ (deg)	ϕ (deg)	$ \langle \vartheta \rangle - \phi $ (deg)	μ ($\mu\text{as y}^{-1}$)	β_{app} (c)	t_{ej}	t_{mid}	α_m (μas)	δ_m (μas)
(1)	(2)	(3)	(4)	(5)	(6)	(7)	(8)	(9)	(10)	(11)	(12)	(13)	(14)	(15)
0003+380	1	8	5	4.23	15.36	120.7	96 \pm 17	24 \pm 17	158 \pm 43	2.30 \pm 0.63	...	2008.81	3691 \pm 74	-2169 \pm 80
0003+380	2	6	19	1.78	6.45	112.6	120.1 \pm 3.1	7.5 \pm 3.1	317 \pm 25	4.61 \pm 0.36	...	2007.71	1662 \pm 29	-694 \pm 11
0003+380	4	5	16	1.25	4.53	114.9	205 \pm 14	90 \pm 14 ^b	39 \pm 10	0.57 \pm 0.15	...	2009.54	1130 \pm 11	-527 \pm 14
0003+380	5	8	40	0.75	2.71	117.5	21 \pm 89	96 \pm 89	2.7 \pm 7.6	0.04 \pm 0.11	...	2010.26	663 \pm 20	-342 \pm 10
0003+380	6	10	98	0.39	1.43	115.4	335 \pm 46	141 \pm 46	12.7 \pm 8.4 ^d	0.19 \pm 0.12	...	2009.90	350 \pm 22	-158 \pm 19
0003-066	2	5	222	1.05	5.12	322.9	226.3 \pm 4.9	96.6 \pm 5.0 ^b	191 \pm 15	4.09 \pm 0.33	...	1997.80	-585.9 \pm 8.9	883 \pm 37
0003-066	3	9	119	2.82	13.73	296.9	284.8 \pm 4.7	12.1 \pm 4.8	250 \pm 39	5.36 \pm 0.83	...	1999.33	-2375 \pm 98	1237 \pm 41
0003-066	4 ^a	26	120	6.61	32.23	285.6	284 \pm 11	2 \pm 11	41 \pm 14	0.87 \pm 0.29	...	2004.83	-6326 \pm 60	1768 \pm 22
0003-066	5 ^a	14	1031	0.70	3.40	10.7	350.9 \pm 5.3	19.9 \pm 5.5 ^b	88.1 \pm 4.3	1.888 \pm 0.091	...	2004.37	138 \pm 18	634.1 \pm 9.0
0003-066	6 ^a	10	97	1.01	4.92	290.2	210 \pm 15	81 \pm 15 ^b	55 \pm 17	1.18 \pm 0.37	...	2003.78	-941 \pm 15	359 \pm 33

^a Acceleration model fit indicates significant accelerated motion.

^b Feature has significant non-radial motion according to the vector motion fit.

^c Feature has significant inward motion according to the vector motion fit.

^d Feature has slow pattern speed.

A question mark indicates a feature whose motion is not consistent with outward, radial motion but for which the possibility of inward motion and its degree of non-radialness are uncertain.

NOTE—Columns are as follows: (1) B1950 name, (2) feature number, (3) number of fitted epochs, (4) mean flux density at 15 GHz in mJy, (5) mean distance from core feature in mas, (6) mean projected distance from core feature in pc, (7) mean position angle with respect to the core feature in degrees, (8) position angle of velocity vector in degrees, (9) offset between mean position angle and velocity vector position angle in degrees, (10) proper motion in $\mu\text{as y}^{-1}$, (11) apparent speed in units of the speed of light, (12) estimated epoch of origin, (13) date of reference (middle) epoch used for fit, (14) fitted right ascension position with respect to the core at the middle epoch in μas , (15) fitted declination position with respect to the core at the middle epoch in μas .

This table is published in its entirety in the machine-readable format. A portion is shown here for guidance regarding its form and content.

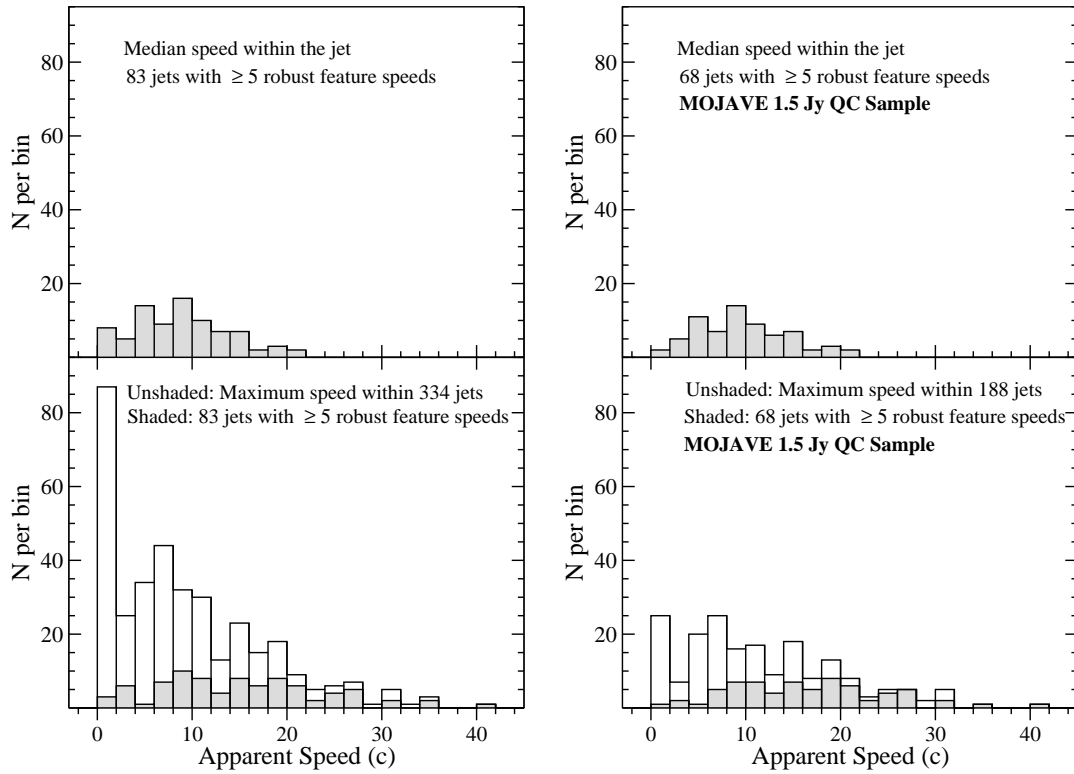


Figure 2. Histogram plots of median jet speed (top panels) and fastest jet speed (bottom panels) for AGN with known redshifts. The histograms in the right hand panels show AGN in the flux density-limited MOJAVE 1.5 Jy QC sample.

Table 6. Acceleration Fit Properties of Jet Features

Source	I.D.	ϕ (deg)	$ \langle\vartheta\rangle - \phi $ (deg)	μ ($\mu\text{as y}^{-1}$)	β_{app} (c)	$\dot{\mu}$ ($\mu\text{as y}^{-2}$)	ψ (deg)	$\dot{\mu}_{\perp}$ ($\mu\text{as y}^{-2}$)	$\dot{\mu}_{\parallel}$ ($\mu\text{as y}^{-2}$)	α_m (μas)	δ_m (μas)
(1)	(2)	(3)	(4)	(5)	(6)	(7)	(8)	(9)	(10)	(11)	(12)
0003+380	6	333 ± 44	142 ± 44	13.4 ± 8.6	0.20 ± 0.12	9.8 ± 8.4	309 ± 53	-4.0 ± 9.4	9.0 ± 9.0	371 ± 33	-175 ± 28
0003-066	4 ^a	277.3 ± 3.8	8.3 ± 3.8	50.9 ± 5.3	1.09 ± 0.11	28.5 ± 2.3	73.7 ± 3.1	11.4 ± 2.1	-26.1 ± 2.5	-6582 ± 32	1693 ± 20
0003-066	5 ^a	353.9 ± 3.0	16.8 ± 3.1 ^b	87.2 ± 4.4	1.868 ± 0.093	26.6 ± 4.9	274 ± 10	-26.3 ± 4.9	4.5 ± 4.8	199 ± 15	630 ± 14
0003-066	6 ^a	211.3 ± 9.6	78.9 ± 9.6 ^b	54 ± 11	1.16 ± 0.24	65 ± 16	336 ± 11	54 ± 13	-37 ± 18	-901 ± 16	268 ± 35
0003-066	8 ^a	290.7 ± 1.6	3.5 ± 1.6	330.4 ± 9.7	7.08 ± 0.21	67 ± 12	127 ± 10	-19 ± 12	-64 ± 12	-2444 ± 30	1121 ± 28
0003-066	9	295.2 ± 4.1	7.5 ± 4.3	278 ± 20	5.96 ± 0.42	99 ± 35	110 ± 22	9 ± 37	-99 ± 35	-1769 ± 52	582 ± 53
0010+405	1	340.7 ± 4.4	11.9 ± 4.4	432 ± 42	6.99 ± 0.68	44 ± 83	147 ± 76	11 ± 53	-43 ± 70	-4259 ± 76	6991 ± 107
0010+405	2	9 ± 123	41 ± 123	2 ± 14	0.04 ± 0.23	4 ± 22	152 ± 123	2 ± 21	-3 ± 23	-898 ± 30	1470 ± 48
0010+405	3	138 ± 83	170 ± 83	2.5 ± 5.4	0.041 ± 0.088	6.9 ± 6.1	99 ± 57	-4.3 ± 8.8	5.4 ± 9.0	-493.6 ± 9.5	783 ± 15
0010+405	4	113 ± 98	145 ± 98	1.4 ± 4.5	0.022 ± 0.072	5.2 ± 8.9	318 ± 69	-2.2 ± 7.1	-4.7 ± 8.1	-240.6 ± 9.0	382 ± 14

^a Feature shows significant accelerated motion.

^b Feature shows significant non-radial motion according to the acceleration fit.

^c Feature shows significant inward motion according to the acceleration fit.

A question mark indicates a feature whose motion is not consistent with outward, radial motion but for which the possibility of inward motion and its degree of non-radialness are uncertain.

NOTE—Columns are as follows: (1) B1950 name, (2) feature number, (3) proper motion position angle in degrees, (4) offset between mean position angle and proper motion position angle in degrees, (5) proper motion in $\mu\text{as y}^{-1}$, (6) apparent speed in units of the speed of light, (7) acceleration in $\mu\text{as y}^{-2}$, (8) acceleration vector position angle in degrees, (9) acceleration perpendicular to velocity direction in $\mu\text{as y}^{-2}$, (10) acceleration parallel to velocity direction in $\mu\text{as y}^{-2}$, (11) fitted right ascension position with respect to the core at the middle epoch in μas , (12) fitted declination position with respect to the core at the middle epoch in μas .

This table is published in its entirety in the machine-readable format. A portion is shown here for guidance regarding its form and content.

Table 7. MOJAVE Jet Properties

B1950	μ_{\max}	μ_{med}	β_{\max}	β_{med}	N_{ep}	N_r	Ref.	$\overline{\text{PA}}$	ΔPA	$\log \text{Var}(\text{PA})$	Δt
(1)	(2)	(3)	(4)	(5)	(6)	(7)	(8)	(9)	(10)	(11)	(12)
0003+380	317 ± 25	...	4.61 ± 0.36	...	10	5	3	115	17	-2.5	7.4
0003-066	330.4 ± 9.7	116 ± 23	7.08 ± 0.21	2.48 ± 0.49	27	9	3	15	12	-2.8	17.3
0006+061	221 ± 43	5	2	6	63	4	-3.5	1.4
0007+106	269 ± 50	...	1.58 ± 0.29	...	25	2	3	292	32	-2.2	12.9
0011+189	159 ± 16	...	4.54 ± 0.46	...	8	2	3	219	3	-3.9	2.1
0010+405	428 ± 40	...	6.92 ± 0.64	...	12	4	3	328	4	-4.0	5.2
0012+610	7.2 ± 6.3 ^a	6	2	6	37	4	-3.5	2.5
0014+813	87.8 ± 8.5	...	9.47 ± 0.91	...	14	3	6	184	22	-2.1	22.7
0015-054	50 ± 20 ^a	...	0.72 ± 0.28 ^a	...	8	1	3	242	16	-2.2	3.5
0016+731	98.5 ± 4.1	...	7.64 ± 0.32	...	16	2	6	126	43	-1.8	24.8
0019+058	257 ± 35	7	2	3	285	14	-2.5	2.6

NOTE—Columns are as follows: (1) B1950 name, (2) maximum jet speed in $\mu\text{as } y^{-1}$, (3) median jet speed in $\mu\text{as } y^{-1}$, (4) maximum jet speed in units of the speed of light, (5) median jet speed in units of the speed of light, (6) number of VLBA epochs, (7) number of robust fitted jet features, (8) reference for jet kinematics, where 1: [Lister et al. \(2013\)](#), 2: [Lister et al. \(2016\)](#), 3: [Lister et al. \(2019\)](#), 4: [Piner et al. \(2010\)](#), 5: [Jorstad et al. \(2017\)](#), 6: this paper, (9) mean innermost jet position angle in degrees, (10) range of innermost jet position angle in degrees, (11) log of circular variance of innermost jet position angle, (12) time coverage used to determine jet position angle statistics in years.

This table is published in its entirety in the machine-readable format. A portion is shown here for guidance regarding its form and content.

^aSpeed is $< 3\sigma$

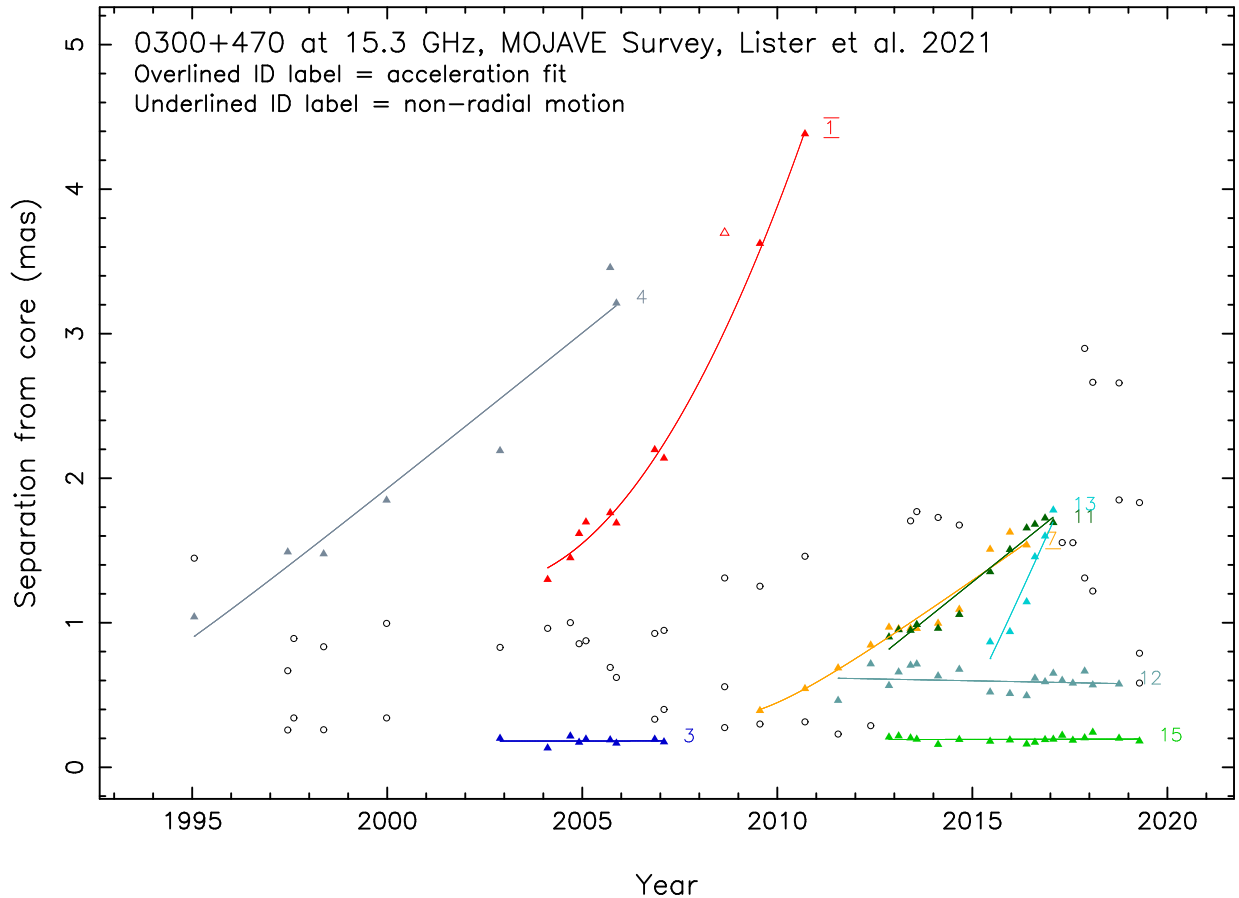


Figure 3. Plot of angular separation from the core versus time for Gaussian jet features. Colored symbols indicate robust features for which kinematic fits were obtained. The identification number is overlined if the acceleration model was fit and indicated a $\geq 3\sigma$ acceleration. An underlined identification number indicates a feature with non-radial motion. The 1σ positional errors on the individual points typically range from 10% of the FWHM restoring beam dimension for isolated compact features, to 20% of the FWHM for weak features. This corresponds to roughly 0.03 mas to 0.15 mas, depending on the declination. (The complete figure set is available in the online journal.)

components from the CLEAN imaging algorithm within an annular region from 0.15 mas to 1 mas from the core. This method fails, however, for AGN with faint jet structure and/or insufficient CLEAN components near the core. Because the method relies on images restored with a Gaussian (natural-weighted) beam, it also does not yield optimal values for many jets in the MOJAVE sample that have sharp apparent bent jet ridge lines near the core. The latter are better traced using the Gaussian model components that are modeled in the visibility plane, which takes advantage of the high positional measurement accuracy of the VLBA for bright features.

We have therefore chosen to use the position of the innermost Gaussian model component with respect to the core to measure the jet PA at each epoch. This generally yields robust results, as exhibited by the good continuity of jet PAs over time in individual AGN. In a few rare cases there are two Gaussian model components

located roughly equidistant from the core, such that the measured PA can alternate between the features over time.

For those source-epochs where the innermost jet feature is robust, we used the residuals in the vector motion fit (or acceleration fit, if a $\geq 3\sigma$ acceleration) to estimate the PA measurement error. For each source-epoch we calculated the standard deviation of the PA distribution of 10 000 simulated locations scattered about the innermost feature position. The scatter in R.A. and declination of these points corresponded to the motion fit residual σ 's of the feature in the respective sky directions.

With this method we were able to estimate a PA measurement error for 5167 of the 7562 source-epochs (68%) for which we tabulated an innermost jet PA. We plot the distribution of these errors in Figure 5. The majority of the values lie between 1° and 10° , with the most common error being $\sim 4^\circ$. A small number of source-epochs

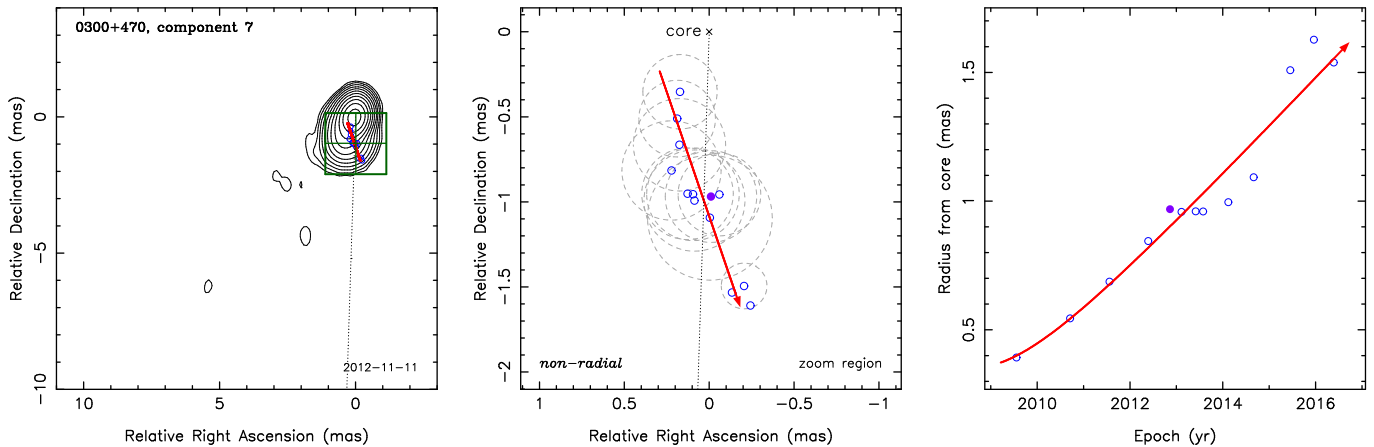


Figure 4. Motion fits and sky position plots of individual robust jet features. Positions are relative to the core position. The left-hand panel shows a 15 GHz VLBA total intensity contour image of the jet at the epoch closest to the middle reference epoch. The green box delimits the zoomed region that is displayed in the middle panel. The feature’s position at the image epoch is indicated by the green cross-hairs. The dotted line connects the feature with the core feature and is plotted with the mean position angle. The position at the image epoch is shown by a filled blue circle while other epochs are plotted with unfilled blue circles. The red solid line indicates the vector fit (or accelerating fit, if there is significant acceleration) to the feature positions. The gray dashed circles or ellipses indicate the fitted FWHM sizes of the feature at the measured epochs. The right-hand panel shows the radial separation of the feature from the core feature over time. (The complete figure set is available in the online journal.)

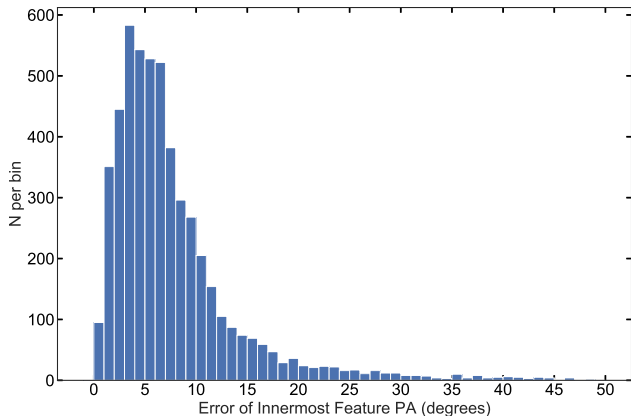


Figure 5. Distribution of innermost jet PA measurement error for all source-epochs.

have large PA error values. Most of these are overestimates, due to features with second-order accelerations that are not well-fit by a constant acceleration model (e.g., PKS 1510–089 id 15, 1641+399 id 12), and therefore have large fit residuals.

3.3.1. Trends with time

We calculated for each jet the circular mean (\overline{PA}), the full range over which the PA varies (ΔPA), and the circular variance. Although the latter quantity formally spans a possible range between $0 \leq \text{Var}(PA) \leq 1$, we use the base 10 logarithm of $\text{Var}(PA)$ as there are a large number of values very close to zero. We list these quantities in Table 7.

To mitigate the possible effects of sampling bias, we restricted our statistical analysis to those jets with 12 or more VLBA epochs over a minimum 10 year period. A total of 173 jets met this criterion, 143 of which are in the MOJAVE 1.5JyQC sample. Most of the jets have inner PAs that vary on decadal timescales over a range of 10° to 50° . However some jets display very large changes in PA, with the overall distribution having a continuous tail out to $\Delta PA = 200^\circ$.

A jet can change its apparent PA over time in several different ways. One way is to eject a feature that moves steadily outward on a curved or non-radial trajectory, resulting in a smooth evolution of the inner jet PA. We show some examples of this in Figure 6. A newly ejected feature may also experience a very rapid fading, reverting the innermost PA to the next feature farther downstream (e.g., IVS B2131–021; Figure 7). In rare cases the inner jet PA can alternate over time between two nearly equidistant downstream features (e.g., IVS B1030+415 and B2 1520+319; Figure 7).

It is also possible for a jet to show a sudden large jump in PA when a new bright feature emerges from the core region at a significantly different position angle from previous ones. An example is 0851+202 (OJ 287), which underwent a monotonic ~ 3 degree per year change in jet PA from 1995 to 2010 due to the non-radial motion of feature id 10. In May 2010 the inner PA jumped $\sim 100^\circ$ when a new bright feature (id 19) emerged from the core region with a substantially different trajectory. Other examples have occurred in the jets

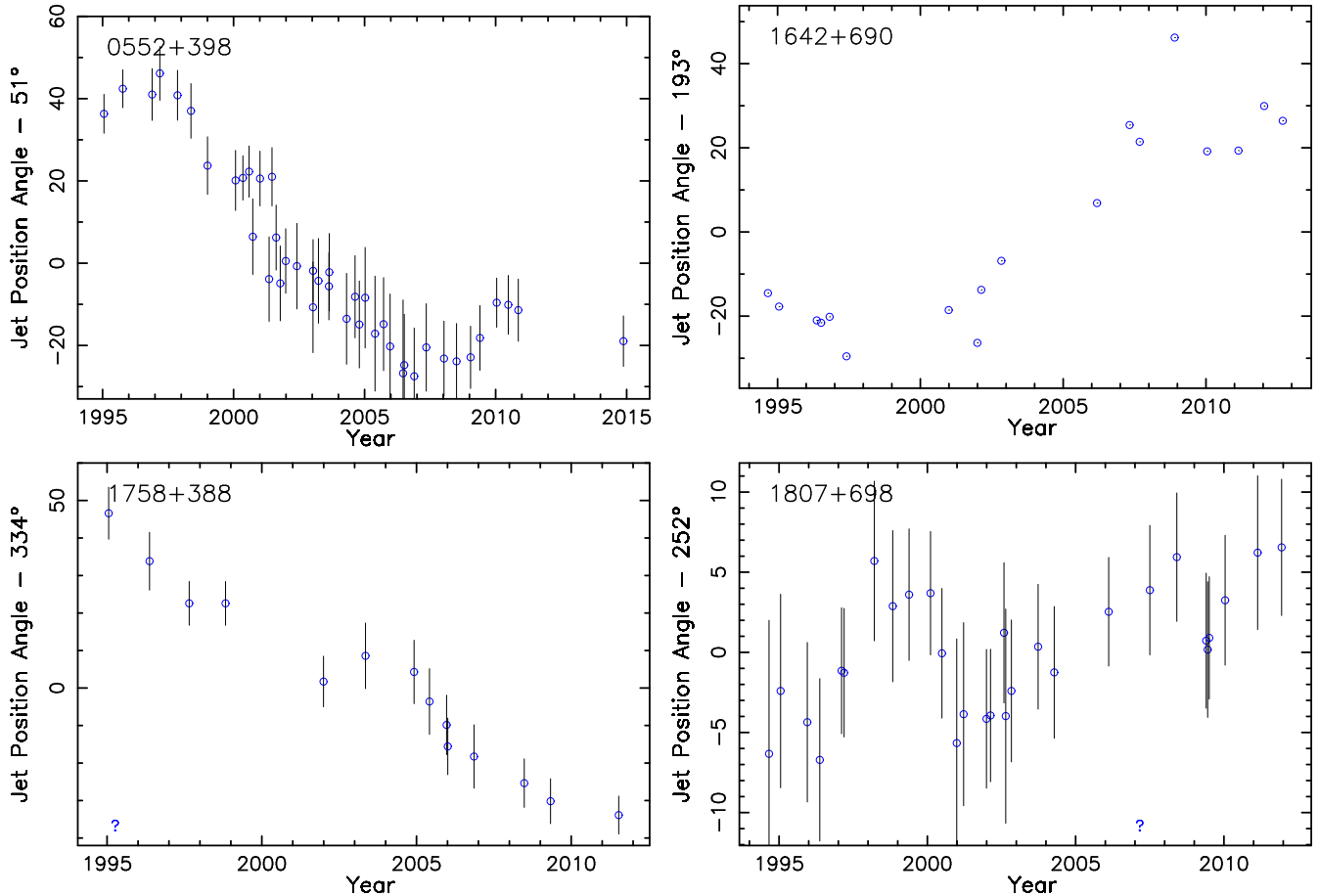


Figure 6. Plots of inner jet PA versus time for selected AGN that show smooth PA evolution due to a feature moving steadily outward on a non-radial or curved trajectory. Error bars are plotted for epochs in which the PA error could be estimated from the kinematic fit residuals for the innermost jet feature. Question marks indicate VLBA epochs for which a PA measurement could not be obtained.

of PKS 0420–014, 1253–055 (3C 279), and 1633+382 (4C +38.41) (Figure 8).

3.3.2. Jet Nozzle Wobbling

There has been extensive discussion in the literature about possible causes of nozzle wobbling in AGN jets (see, e.g., review by Qian et al. 2014), which include MHD flow instabilities (Matveyenko & Seleznev 2015), Lense-Thirring precession of the accretion disk (Liu & Melia 2002; Caproni et al. 2004), or the influence of a binary black hole companion (Dey et al. 2021). Precession is well-characterized in stellar jet systems such as SS 433 (Roberts et al. 2008), but the much longer timescales and vastly larger distances associated with AGN jets and their accretion disks make their study more challenging.

A complicating factor in using VLBI data to investigate jet precession is that we are not seeing the full extent of the jet. Our long term monitoring has shown that at any given epoch, only certain portions of the flow are sufficiently energized to appear in VLBA images,

which typically have dynamic ranges of a few thousand to one (Lister et al. 2013). A good example is the quasar 1308+326 (OP 313), which in the mid 1990s showed no apparent downstream jet emission on parsec scales (Ojha et al. 2004). Throughout the following 25 years this AGN launched a series of bright features that moved downstream on trajectories with a variety of individual position angles, giving an illusory bent jet appearance in individual epoch images. When the images over a 25 year period are stacked, however, a smooth conical jet structure emerges (Pushkarev et al. 2017). In the case of 1308+326, the axis of the broader outflow has remained relatively stable, but the inner jet PA has varied by $\sim 85^\circ$ due to individual emerging features that do not fill the entire jet cross-section.

To look for possible evidence of nozzle wobbling, we examined 24 jets in our sample that display overall monotonic trends of 10 years or more in their PA evolution. In 11 cases, the evolution is caused by one or more jet features moving on non-radial or curved tra-

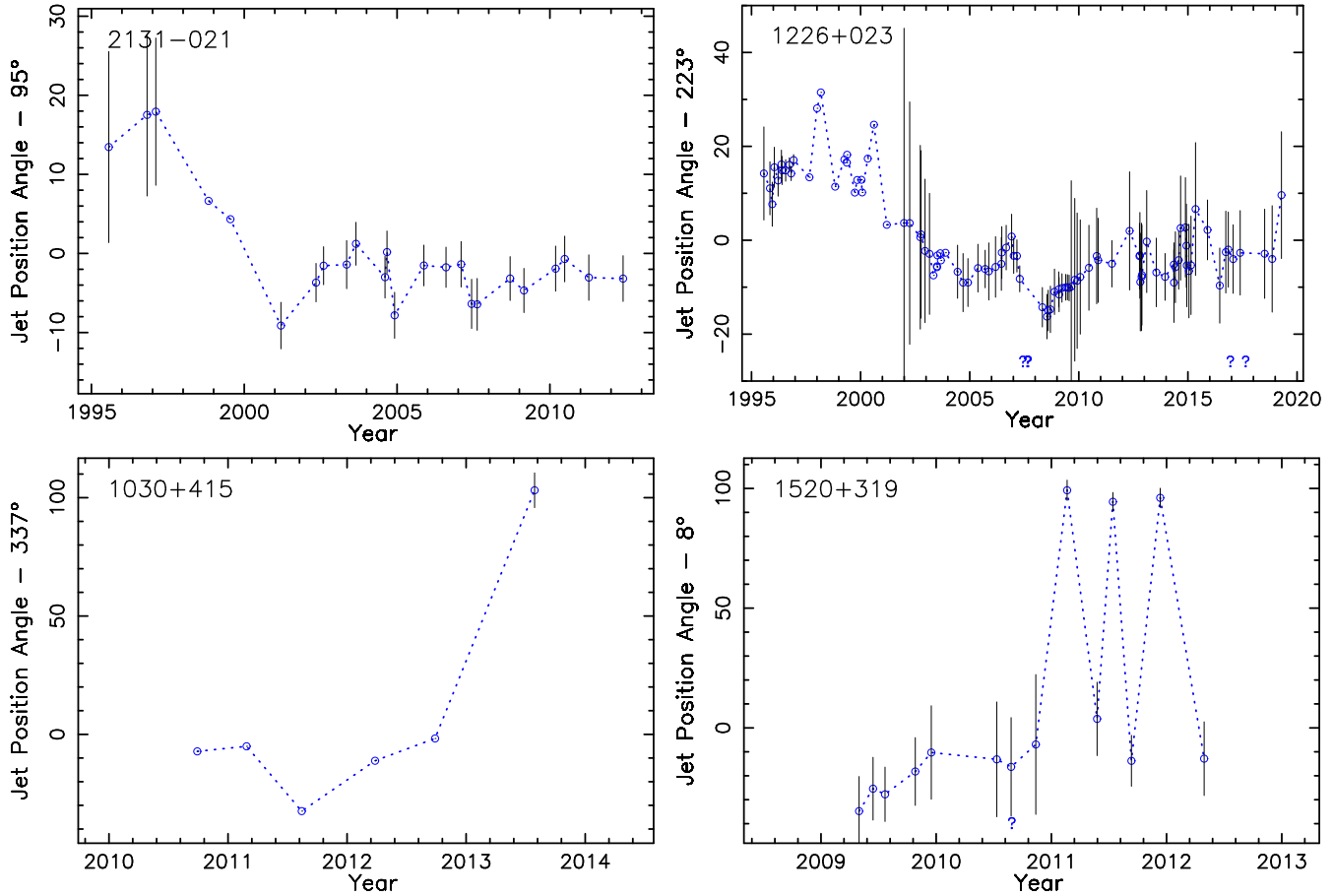


Figure 7. Plots of inner jet PA versus time for selected individual AGN. In IVS B2131–021 the PA changed in 2001 due to the emergence of a new jet feature (id 5). The jet of 1226+023 (3C 273) showed a decade long steady evolution of jet PA from 1995 to 2005, while 11 separate features emerged from the core region during this time interval. The jets of IVS B1030+415 and B2 1520+319 contain features with position angles differing by $\sim 100^{\circ}$ that are nearly equidistant from the core, causing the innermost PA to alternate between them at different epochs.

jectories. In the remaining 13 AGN, however, multiple features emerge from the core over time, yet there is an overall monotonic evolution of the jet PA. In other words, the ejection directions of successive features are not random, but follow a systematic trend. One example is 0430+052 (3C 120), for which we have sufficient spatial resolution ($z = 0.033$; 0.65 pc per mas) to track the motions of many features that are ejected at a rate of roughly one per year. Over a 25 year period, the initial PAs of successive features have progressed steadily from $\sim 231^{\circ}$ to $\sim 256^{\circ}$. The bright nearby quasar 1226+023 (3C 273; $z = 0.1583$) has also displayed an overall swing in ejection PAs from $\sim 237^{\circ}$ in 1995 to $\sim 208^{\circ}$ in 2008. After 2008, its inner jet PA remained relatively stable at $\sim 220^{\circ} \pm 10^{\circ}$ (Figure 7).

Because the ejected features do not fill the entire jet cross-section in observed emission, a wobbling flow instability generated near the jet base is the most likely mechanism for the observed PA variations in many jets. As this region of enhanced magnetic field strength

and/or plasma density precesses, new jet features are launched at different locations within a broader outflow of typical full opening angle $\sim 1^{\circ} - 4^{\circ}$ (Section 3.3.3). Occasionally this instability may be disrupted and/or a new instability forms at another location, resulting in a sudden jump in jet PA, as seen in OJ 287. Wang et al. (2021) describe a similar scenario for the nearby radio-quiet quasar Mrk 231, in which they report a $\sim 60^{\circ}$ change in pc-scale jet position angle over a 25 year period. In their model the jet occupies a wide angle cone, and the bright knots represent the active working surface of the jet head hitting the interstellar medium.

Several jets in our sample have very large PA ranges ($> 150^{\circ}$): B2 0202+319, 0355+508 (NRAO 150), S4 1144+402, B3 1417+385, PKS 1622–253, 2028+492 (87GB 202807.5+491605), which may be indicative of a viewing angle inside the jet opening angle. Since the individual moving features do not fill the entire jet cross section, such jets would be expected to display a wide range of ejection position angles.

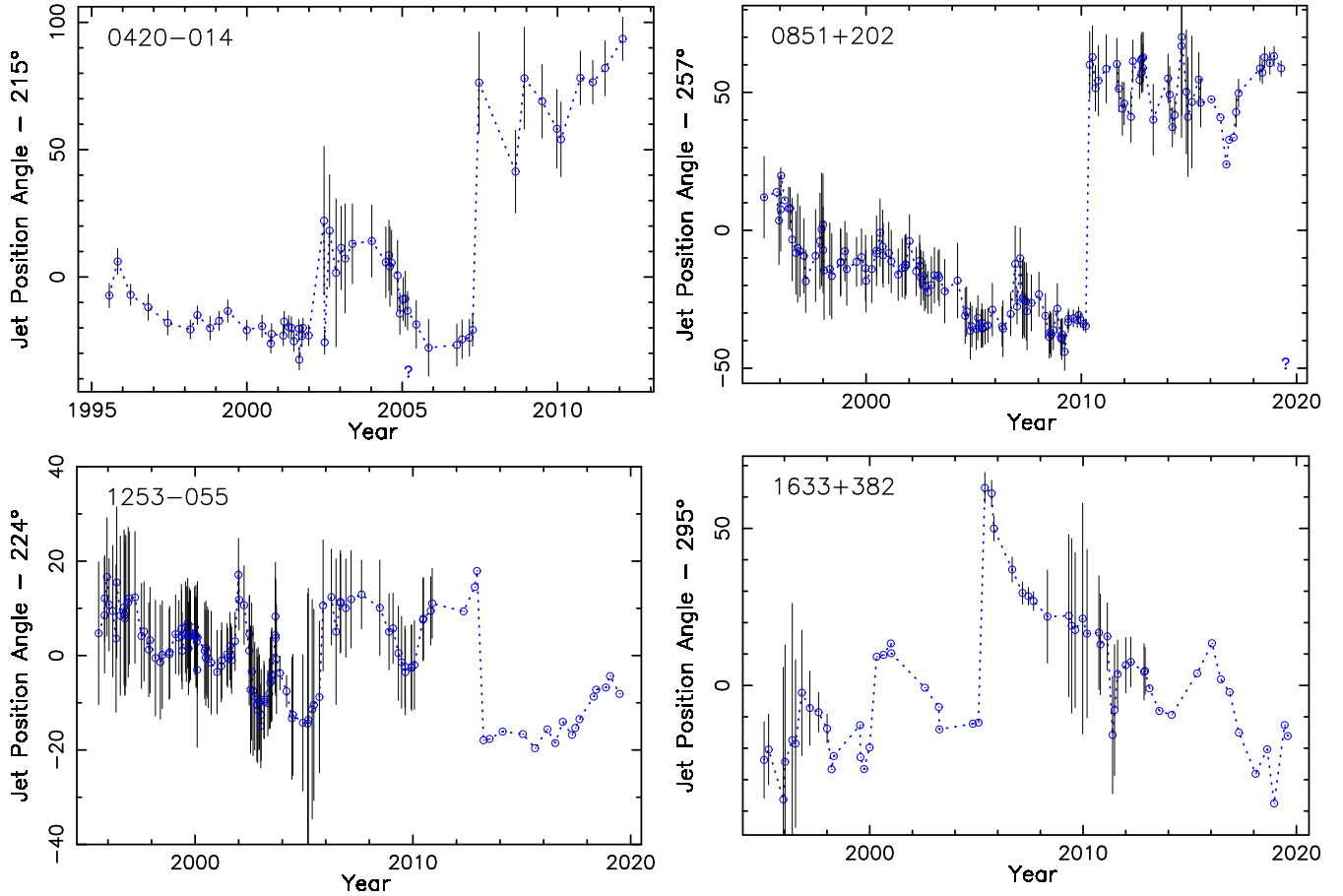


Figure 8. Plots of inner jet PA versus time for several individual AGN that show sudden jumps in PA due to the emergence of a new feature with a substantially different trajectory than previous features. This occurred in 2002 and 2007 for 0420-014, in 2010 for 0851+202 (OJ 287), in 2005 and 2013 for 1253-055 (3C 279), and in 2005 for 1633+382.

If the main axis of the broad outflow remains stable over time, a wobbling jet instability could appear as an oscillatory PA trend in our data, provided that the precession period is smaller than our time coverage (up to 25 years for the most heavily observed jets). In [Lister et al. \(2013\)](#) we reported 12 jets with possible oscillating PAs, but the fitted periods of 5 yr to 12 yr were too long to establish any periodicity.

Of the 173 jets in our sub-sample with good epoch coverage, 67 show possible back and forth PA evolution. We used the Lomb-Scargle periodogram algorithm for unequally sampled data ([Lomb 1976](#); [Scargle 1982](#)) to look for possible periodicities. We plot the best fit sinusoid cases in [Figure 9](#). The jet with the lowest reduced χ^2 fit value is 0738+313 (OI 363), but the fitted period of 16.7 yr is comparable to the 24 yr range of the data. The other fits in [Figure 9](#) have larger χ^2 values due to departures from pure sinusoidal periodic behavior. The best fit periods range from 6 yr to 16.7 yr. Given that these are comparable to the length of our VLBA coverage, it is not possible with our current data set to robustly

claim PA periodicity in any of the jets in our sample. We note that 8 of the 12 oscillating PA jets we reported in [Lister et al. \(2013\)](#): PKS 0754+100, 1308+326, PKS 1335-127, 1611+343 (DA 406), 1730-130 (NRAO 530), S5 1803+784, PKS 2134+004, 2145+067 (4C +06.69) do not show sinusoidal periodicity, based on our new PA determinations and/or the addition of new VLBA epochs.

3.3.3. Trends with AGN Classes

We have examined the PA range and variance statistics with respect to general AGN properties using Anderson-Darling tests ([Stephens 1974](#)). Our sub-sample is made up of 117 quasars, 43 BL Lacs, 10 radio galaxies, and 3 narrow-line Seyfert Is. All but 18 of these AGN have been listed as *Fermi* LAT gamma-ray associations ([Table 1](#)).

With respect to optical classification, we find that BL Lacs have smaller PA ranges ($p_{\text{null}} = 0.0037$) and PA variances ($p_{\text{null}} = 0.001$) than quasars ([Figure 10](#)). Our tests indicate that these two sub-samples have indistinguishable VLBA epoch coverage, but substantially

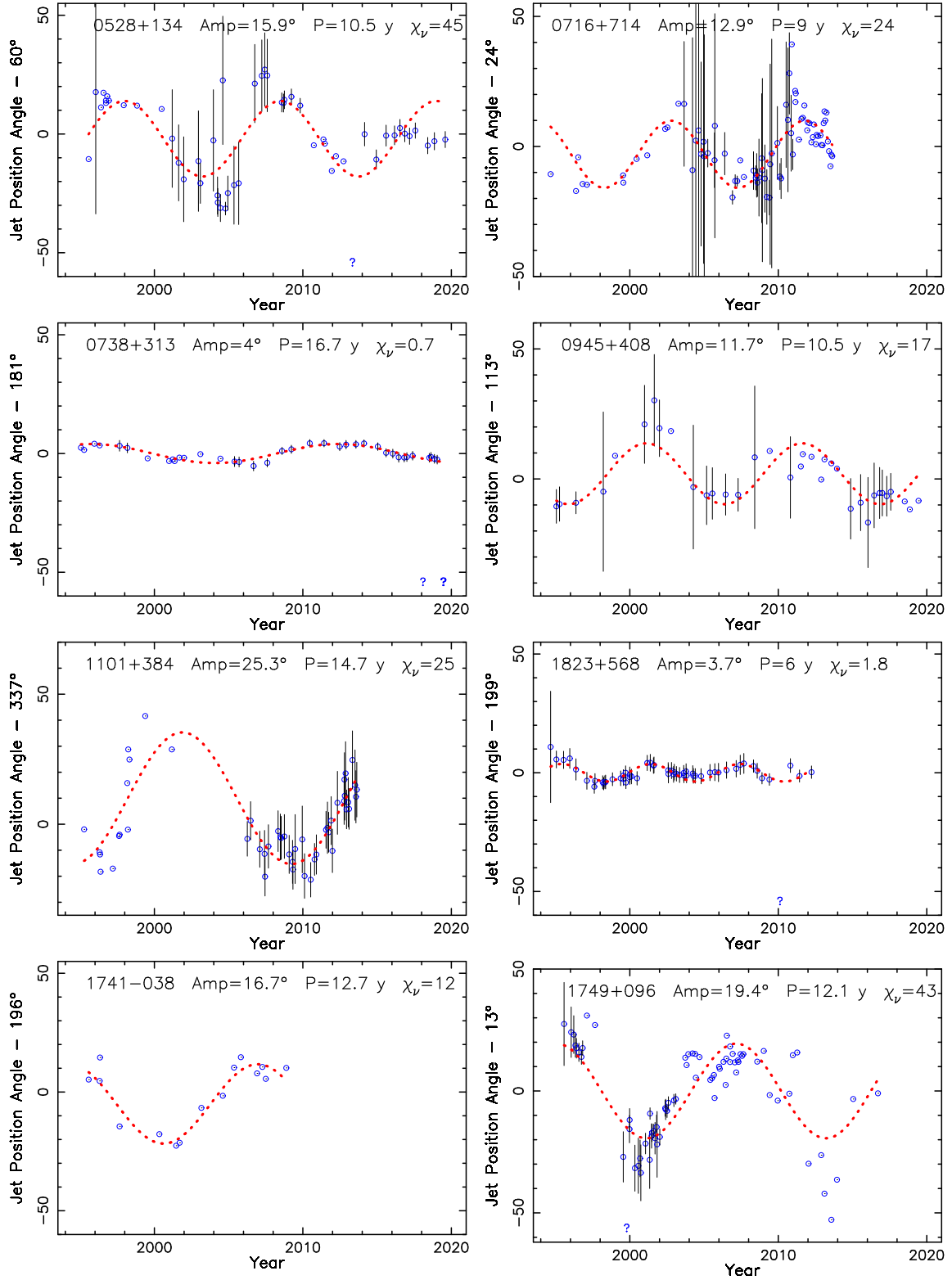


Figure 9. Plots of inner jet PA versus time for individual AGN (blue circles) overplotted with best fit sinusoid curves (red dotted lines). These represent the best cases in the sample for possible periodicity. Each panel is plotted with the same vertical scaling for comparison purposes.

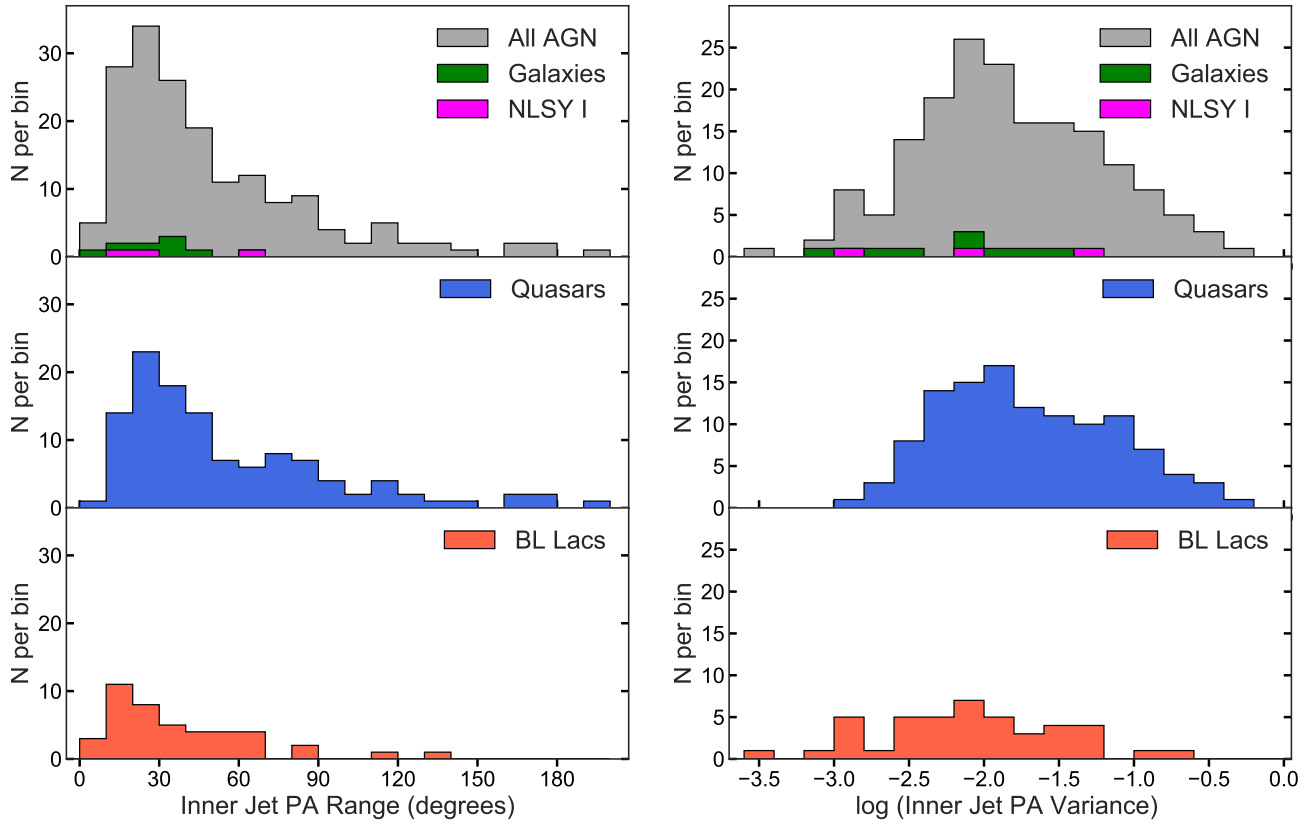


Figure 10. Distributions of inner jet PA range (left panel) and variance (right panel) for different AGN optical classes.

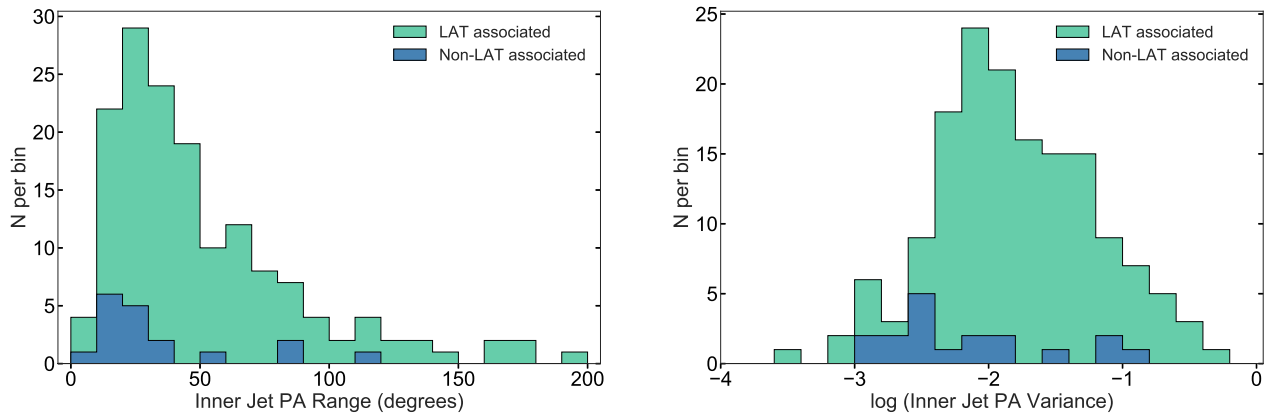


Figure 11. Distributions of inner jet PA range (left panel) and variance (right panel) for LAT associated and non-LAT associated AGN.

different redshift distributions, with the BL Lacs having generally lower z values. It is unlikely that the PA differences are due to redshift, however, since we find (i) no trend of ΔPA with z within the quasar sub-sample (which spans $0.16 < z < 3.4$) and (ii) no significant difference in the ΔPA distributions of quasars and radio galaxies, where the latter are all at low redshift ($0.004 < z < 0.14$).

We do not find any statistically significant differences in the PA ranges or PA variances of the 23 TeV-detected AGN compared to the other AGN in our sample. However, we find that the 18 non-LAT associated AGN have smaller PA ranges ($p_{\text{null}} = 0.0098$) and PA variances ($p_{\text{null}} = 0.0076$) than the LAT associated AGN (Figure 11). There are no significant differences in the epoch coverage or redshift distributions of the LAT vs. non-LAT AGN.

There are several possible factors that could increase the range and variance of a jet’s PA over time, including a wider apparent opening angle of its overall plasma outflow, and a less stable jet base. Also, as more emerging features are tracked in a jet over time, the spread of initial trajectory position angles (ΔPA) may be expected to increase until it approaches the full jet opening angle. The BL Lacs, quasars, LAT and non-LAT AGN show no significant differences in their number of robust jet features, which suggests that the feature ejection rate (which is not affected by Doppler time compression effects) does not have a strong influence on the PA variance. We have also ruled out the possible effects of observational time coverage and redshift based on our statistical tests. The remaining factors to consider are the intrinsic nozzle stability, intrinsic opening angles, and viewing angles of the jets.

In a previous analysis of the MOJAVE sample (Lister et al. 2015) we found that the non-*Fermi* LAT associated AGN tend to have lower Doppler boosting factors and spectral energy distributions (SED) that are peaked at lower frequencies. All of the 43 BL Lacs in our sub-sample are LAT-associated, which is consistent with their generally harder gamma-ray spectra and SED peaks that span a large range, up to 10^{17} Hz. The non-LAT radio galaxies and quasars, on the other hand, have SED peaks that range up to only $10^{13.4}$ Hz.

In Figure 12 and 13 we plot $\text{Var}(\text{PA})$ and ΔPA versus the SED peak frequency for the 174 AGN in our sub-sample. The non-LAT associated AGN are plotted with filled symbols. There is a tendency for lower synchrotron peaked AGN to have more variable inner jet PAs ($p_{\text{null}} = 0.006$ for ΔPA and $p_{\text{null}} = 0.0003$ for $\text{Var}(\text{PA})$), according to Spearman’s ρ tests).

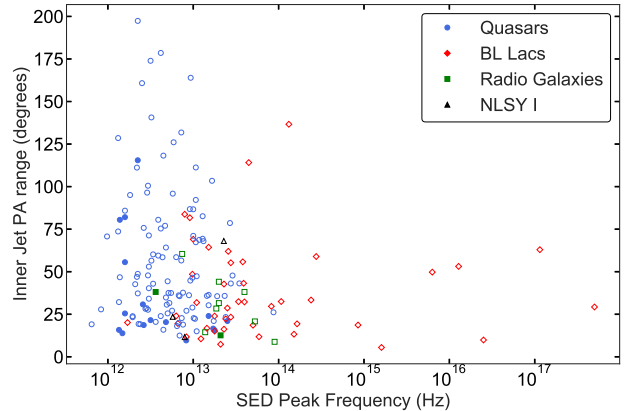


Figure 12. Scatter plot of ΔPA versus SED peak frequency for the 174 AGN in our statistical sub-sample. The filled symbols indicate non-LAT associated AGN.

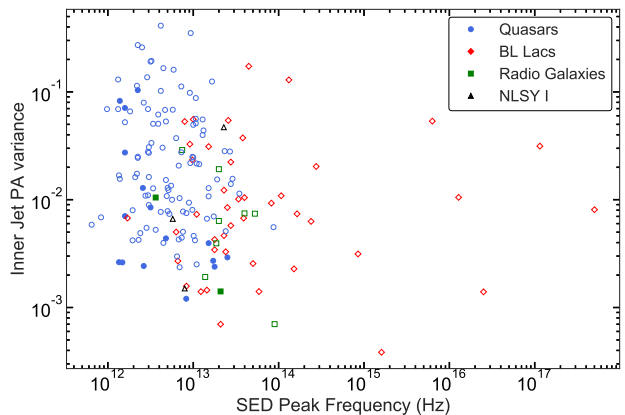


Figure 13. Scatter plot of PA variance versus SED peak frequency for the 174 AGN in our statistical sub-sample. The filled symbols indicate non-LAT associated AGN.

We have determined Doppler factors (δ) for the jets in our sample as part of a MOJAVE study of core brightness temperatures (Homan et al., in prep.). The latter follows on our previous work (Homan et al. 2006) and exploits the fact that in their median low-brightness temperature (T_b) state, the MOJAVE AGN cores have a narrow range of intrinsic T_b values (T_{int}). Homan et al. derive Doppler factors from the observed T_b values according to $T_{\text{obs}} = \delta T_{\text{int}}$, and jet viewing angles (θ) from the maximum measured jet speeds presented in this paper.

The jets in our sample with $\delta \lesssim 10$ show a smaller range of jet PA (Figure 14) and PA variance (Figure 15). This is primarily a consequence of their larger jet viewing angles. As a conical jet is oriented closer to the plane of the sky ($\theta \rightarrow 90^\circ$), its apparent half opening angle ϕ_{app} will approach its intrinsic half opening angle

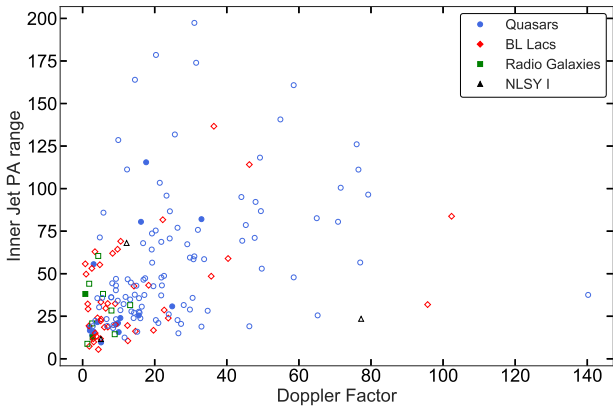


Figure 14. Scatter plot of inner jet PA range versus Doppler factor for different optical classes, with quasars = blue circles, BL Lacs = red diamonds, radio galaxies = green squares, NLSY1 = black triangles. Filled symbols indicate non-LAT associated AGN.

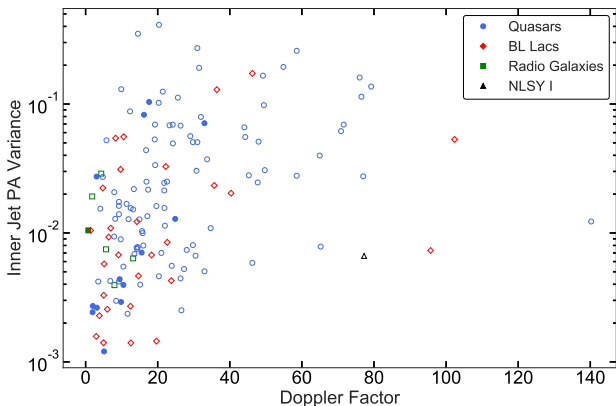


Figure 15. Scatter plot of PA variance versus Doppler factor for different optical classes, with quasars = blue circles, BL Lacs = red diamonds, radio galaxies = green squares, NLSY1 = black triangles. Filled symbols indicate non-LAT associated AGN.

ϕ , where

$$\tan \phi_{\text{app}} = \frac{\tan \phi}{\sin \theta} \left(1 - \frac{\tan^2 \phi}{\tan^2 \theta} \right)^{-1/2}. \quad (1)$$

Conversely, as a conical jet is oriented closer to the line of sight, it will be viewed inside its opening angle when $\theta \leq \phi$.

In Figure 16 we plot the inner jet PA range versus jet viewing angle. A Spearman non-parametric test indicates a strong trend ($p_{\text{null}} = 10^{-10}$) of smaller PA ranges for jets viewed farther from the line of sight. We have over-plotted dashed curves showing the full apparent jet opening angle as a function of viewing angle θ for several values of intrinsic half opening angle. We have

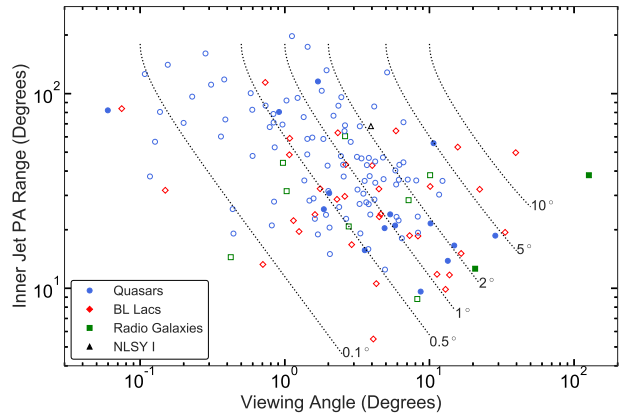


Figure 16. Scatter plot of inner jet PA range versus viewing angle for different optical classes, with quasars = blue circles, BL Lacs = red diamonds, radio galaxies = green squares, NLSY1 = black triangles. Filled symbols indicate non-LAT associated AGN. The dotted curves indicate the apparent full opening angle of a conical jet as a function of viewing angle, for different values of intrinsic half opening angle as indicated.

truncated the top of each plotted curve at $\theta = \phi$, beyond which the expected apparent PA range increases to 360° . As evident from Figure 16, the majority of the jets have intrinsic half opening angles between $\sim 0.5^\circ$ and $\sim 2^\circ$.

It can be seen in Figure 16 that there are no obvious differences in the intrinsic jet opening angles of the BL Lacs versus quasars. The BL Lacs in the MOJAVE sample are a mixture of low- and high-spectral peaked blazars, with the latter generally having lower Lorentz factors, lower Doppler factors, and larger viewing angles than the quasars (Homan et al., ApJ, submitted). We conclude that the overall larger viewing angles of BL Lac jets are responsible for their smaller jet PA ranges and variances.

The LAT and non-LAT associated AGN have a similar intrinsic median opening angle, although we note there is only one non-LAT jet (PKS 0607–15) narrower than 0.4° . The non-LAT jets have larger viewing angles ($p_{\text{null}} = 0.002$) and lower Doppler factors ($p_{\text{null}} = 0.003$). Their respective Lorentz factor distributions have a marginal probability ($p_{\text{null}} = 0.04$) of being drawn from the same population. As it was in the case of the BL Lacs versus quasars, the non-LAT jets have smaller PA ranges and variances than LAT-associated AGN because they are oriented at larger angles to the line of sight.

4. SUMMARY AND CONCLUSIONS

We have analyzed the parsec-scale jet kinematics of 447 bright radio-loud AGN based on 15 GHz VLBA

data obtained between 1994 August 31 and 2019 August 4. This represents the largest and most complete AGN jet kinematics study to date. These northern sky AGN (J2000 declination $> -30^\circ$) have been part of the 2cm VLBA survey or MOJAVE programs, and have correlated flux density > 50 mJy at 15 GHz. There are 49 AGN that have not appeared in previous MOJAVE kinematics papers. These were added on the basis of their gamma-ray emission properties or membership in the Robopol optical polarization monitoring program. We present new total intensity and linear polarization maps obtained between 2017 January 1 to 2019 August 4 for 143 AGN in our sample.

By modeling the jet emission with a series of Gaussians in the interferometric visibility plane, we identified and tracked 1923 individual features over at least five epochs. We fitted their sky trajectories with simple radial and vector motion models, and additionally carried out constant acceleration fits for 926 features that had ten or more epochs.

We summarize our findings as follows:

1. We tracked at least one robust bright jet feature across five or more epochs in 419 of the 447 AGN jets in our analysis. A majority (60%) of the well-sampled jet features showed evidence of either accelerated or non-radial motion at the $\geq 3\sigma$ level.

2. Only 2.5% of the robust jet features had velocity vectors apparently directed inward toward the core. However, 8.7% of the AGN jets in the sample had at least one inward-moving feature. These features may be the result of centroid shifts in diffuse emission regions, or curved trajectories crossing the line of sight.

3. We identified 64 non-accelerating features with unusually slow pattern speeds ($\mu < 20 \mu\text{as y}^{-1}$ and at least 10 times slower than the fastest feature in the jet) in 47 jets that may be standing shocks in the flow.

4. We have analyzed variations of the innermost jet position angles in our AGN sample over time. We restricted our analysis to 173 jets that had 12 or more VLBA epochs over a minimum 10 year period. By using the PA of the closest fitted Gaussian feature to the core at each epoch, we derived a mean jet PA, as well as the range of jet PA and its circular variance. Most of the jets have inner PAs that vary on decadal timescales over a range of 10° to 50° . However some jets display very large changes in PA, with the overall distribution having a tail out to $\Delta PA = 200^\circ$. Some jets show a monotonic evolution of PA after ejecting a feature that moves outward on a curved or non-radial trajectory. In some cases, a jet experiences a sudden large jump in PA when a new bright feature emerges with a substantially different trajectory than previously ejected features.

5. We find that AGN with SEDs peaked at lower frequencies tend to have more variable jet PAs. This is reflected in a tendency for the BL Lacs in our sample to have less variable PAs, since their SED peak distribution extends to much higher frequencies than the quasars and radio galaxies. Furthermore, the *Fermi* LAT gamma-ray associated AGN in our sample tend to have more variable PAs than the non-LAT AGN. We have ruled out the possible effects of redshift, time sampling, and feature ejection rate as the cause of these differences. By using Lorentz factor and Doppler factor measurements from a MOJAVE analysis of AGN core brightness temperatures (Homan et al., ApJ, submitted), we conclude that the non-LAT and higher synchrotron peaked (BL Lac) jets show smaller variance and range in their inner jet PAs because they are viewed at slightly larger angles to the line of sight.

6. We have identified 13 AGN where over a decade long period, multiple features emerge from the core with ejection PAs that follow a systematic trend. Since the ejected features do not fill the entire jet cross-section, this behavior is indicative of a wobbling flow instability near the jet base. New features may emerge from this region of enhanced magnetic field/plasma density as it precesses on \sim decadal timescales. Occasionally this instability may be disrupted and/or a new instability forms at another location, resulting in a sudden jump in the inner jet PA. We have looked for evidence of periodic PA behavior in 67 jets that show back and forth PA evolution using Lomb-Scargle periodograms. The best fit periods range from 6 y to 16.7 y, however, we cannot claim any bona fide cases of periodicity since these periods are comparable to the 10 y – 25 y VLBA time coverages of the AGN.

We thank the anonymous referee for helpful comments that improved the manuscript. The MOJAVE project was supported by NASA-*Fermi* grants 80NSSC19K1579, NNX15AU76G and NNX12A087G. YYK is supported in the framework of the State project “Science” by the Ministry of Science and Higher Education of the Russian Federation under the contract 075-15-2020-778. TS was supported by the Academy of Finland projects 274477 and 315721. The Very Long Baseline Array and the National Radio Astronomy Observatory are facilities of the National Science Foundation operated under cooperative agreement by Associated Universities, Inc. This work made use of the Swinburne University of Technology software correlator (Deller et al. 2011), developed as part of the Australian Major National Research Facilities Programme and operated under licence. This research has used observations with RATAN-600 of the Special Astrophysical Observatory, Russian Academy of Sciences (SAO RAS). The observations with the SAO RAS telescopes are supported by the Ministry of Science and Higher Education of the Russian Federation. This research has made use of data from the OVRO 40-m monitoring program Richards et al. (2011), which is supported in part by NASA grants NNX08AW31G, NNX11A043G, and NNX14AQ89G and NSF grants AST-0808050 and AST-1109911. This research has made use of data from the University of Michigan Radio Astronomy Observatory which has been supported by the University of Michigan and by a series of grants from the National Science Foundation, most recently AST-0607523. This research has made use of the NASA/IPAC Extragalactic Database (NED) which is operated by the Jet Propulsion Laboratory, California Institute of Technology, under contract with the National Aeronautics and Space Administration.

Facilities: VLBA, OVRO:40m, RATAN, UMRAO, NED, ADS

Software: astropy (Astropy Collaboration et al. 2013, 2018), DIFMAP (Shepherd 1997), AIPS (Greisen 2003)

APPENDIX

A. NOTES ON INDIVIDUAL AGN

Here we provide comments on individual AGN supplementing those given in Lister et al. (2013), Lister et al. (2016), and Lister et al. (2019).

0106+678 (4C +67.04): An additional VLBA epoch in 2019 has shown that a jet feature (id 4) in this BL Lac no longer has statistically significant inward motion.

0420+417 (4C +41.11): With the addition of new epochs after 2017.0, the centroid of the large diffuse feature (id 6) at the end of the jet shows inward motion. The evolution of the innermost feature (id 11) is not consistent with radial, outward motion.

0518+211 (RGB J0521+212): Additional epochs obtained since 2017.0 indicate that the innermost jet feature in this BL Lac object (id 10) no longer has statistically significant inward motion in the vector fit, but continues to be inward in the acceleration fit.

S4 0636+680: This quasar at $z = 3.177$ has a radio spectrum peaked at 5 GHz, and compact radio structure ~ 1 mas in extent. We assume the core lies in the northernmost feature, which has the highest brightness temperature and flux density.

PKS B0742+103: This quasar has a radio spectrum peaked at 3 GHz, and an uncertain core location in our 15 GHz images. We therefore classified none of the jet features as robust. We assigned the core to the brightest jet feature at each epoch, which lies in between two features (id 4 and id 5). A recent 43 GHz VLBA image by Cheng et al. (2020) shows a core-dominated morphology with jet emission to the N and NW.

0743–006 (OI –072): This quasar at $z = 0.996$ has a radio spectrum peaked at 7 GHz and compact radio structure only 2 mas in extent. A VLBA 43 GHz by Cheng et al. (2020) shows the brightest feature at the southern end of the jet, which we use as the core location for our kinematics analysis.

0810+646 (87GB 081008.0+644032): This BL Lac at $z = 0.239$ had no bright robust jet features.

MRC 0910–208: None of the jet features in this quasar at $z = 0.198$ were sufficiently bright or compact to be labeled as robust.

1101+384 (Mrk 421): Two features (id 9 and id 11) show significant inward motion in the vector motion fit but not in the acceleration fit. Another feature (id 8) has inward motion in both fits.

PKS 1118–056: New epochs obtained after 2017.0 show a new feature (id 8) to have inward motion.

1142+198 (3C 264): Additional kinematics analyses of the VLBA data on this AGN jet have been published by Archer et al. (2020) and Boccardi et al. (2019).

1253–055 (3C 279): The VLBA epochs in 2013–2014 and 2018 April 22 are affected by the emergence of very bright features (> 10 Jy). After these features were ejected they faded rapidly and moved downstream, passing through the quasi-stationary core. Thus the location of the ‘true’ jet core (which is normally too weak to be seen) was briefly revealed. The reference ‘core’ position that we use in this jet at all epochs is likely a strong quasi-stationary feature in the downstream flow. Our interpretation is based on the resulting consistent/continuous sky trajectories of features 5,13, and 14 during 2013–2018 if the quasi-stationary feature is used as a reference point.

1509+054 (PMN J1511+0518): This radio galaxy has two-sided jet structure (Oriente et al. 2006). We have assumed the eastern jet is the approaching one, based on its faster apparent speed (id 3).

1652+398 (Mrk 501): One jet feature (id 5) has significant inward motion in the acceleration fit, but not in the vector model fit.

PKS 1725+123: The addition of new epochs obtained since 2017.0 establish inward motion in one feature (id 2).

1754+155 (87GB 175437.6+153548): We could not identify any robust jet features in this quasar at $z = 2.06$.

1928+738 (4C +73.18): In 2012 an apparent counter-jet feature (id 17) with an apparent speed of $0.4 c$ emerged in this quasar jet. This was followed by another feature (id 21) that appeared in 2017 farther upstream from the core, with no statistically significant motion ($20 \pm 20 \mu\text{as } \text{y}^{-1}$). Given the fast superluminal speeds in the approaching jet ($8.4 c$) and expected large de-boosting of the receding jet emission, these observations suggest that these aren’t true counterjet features, and that the true core in this quasar is visible only at some epochs.

2013–092 (PMN J2016–0903): All of the jet features in this BL Lac with unknown redshift were too faint to be considered robust.

2115+000 (PMN J2118+0013): The radio structure of this narrow-lined Sy 1 galaxy at $z = 0.463$ from the *Fermi* hard-spectrum sample was too compact to identify any robust jet features.

2234+282 (CTD 135): A 43 GHz VLBA image by Cheng et al. (2020) indicates that the core is located at the extreme southwest end of the jet.

S5 2353+816: No robust jet features could be identified in this BL Lac object due to the large gap in the VLBA time coverage.

REFERENCES

- Abdo, A. A., Ackermann, M., Ajello, M., et al. 2009a, ApJ, 707, 55, doi: [10.1088/0004-637X/707/1/55](https://doi.org/10.1088/0004-637X/707/1/55)
- . 2009b, ApJL, 707, L142, doi: [10.1088/0004-637X/707/2/L142](https://doi.org/10.1088/0004-637X/707/2/L142)
- . 2010, ApJS, 188, 405, doi: [10.1088/0067-0049/188/2/405](https://doi.org/10.1088/0067-0049/188/2/405)
- Abdollahi, S., Acero, F., Ackermann, M., et al. 2020, ApJS, 247, 33, doi: [10.3847/1538-4365/ab6bcb](https://doi.org/10.3847/1538-4365/ab6bcb)
- Acero, F., Ackermann, M., Ajello, M., et al. 2015, ApJS, 218, 23, doi: [10.1088/0067-0049/218/2/23](https://doi.org/10.1088/0067-0049/218/2/23)
- Ackermann, M., Ajello, M., Allafort, A., et al. 2011, ApJ, 743, 171, doi: [10.1088/0004-637X/743/2/171](https://doi.org/10.1088/0004-637X/743/2/171)

- Ackermann, M., Ajello, M., Atwood, W. B., et al. 2015, *ApJ*, 810, 14, doi: [10.1088/0004-637X/810/1/14](https://doi.org/10.1088/0004-637X/810/1/14)
- . 2016, *ApJS*, 222, 5, doi: [10.3847/0067-0049/222/1/5](https://doi.org/10.3847/0067-0049/222/1/5)
- Ajello, M., Atwood, W. B., Baldini, L., et al. 2017, *ApJS*, 232, 18, doi: [10.3847/1538-4365/aa8221](https://doi.org/10.3847/1538-4365/aa8221)
- Ajello, M., Angioni, R., Axelsson, M., et al. 2020, *ApJ*, 892, 105, doi: [10.3847/1538-4357/ab791e](https://doi.org/10.3847/1538-4357/ab791e)
- Aller, M. F., Aller, H. D., & Hughes, P. A. 2003, *ApJ*, 586, 33, doi: [10.1086/367538](https://doi.org/10.1086/367538)
- Archer, A., Benbow, W., Bird, R., et al. 2020, *ApJ*, 896, 41, doi: [10.3847/1538-4357/ab910e](https://doi.org/10.3847/1538-4357/ab910e)
- Arsioli, B., & Polenta, G. 2018, *A&A*, 616, A20, doi: [10.1051/0004-6361/201832786](https://doi.org/10.1051/0004-6361/201832786)
- Astropy Collaboration, Robitaille, T. P., Tollerud, E. J., et al. 2013, *A&A*, 558, A33, doi: [10.1051/0004-6361/201322068](https://doi.org/10.1051/0004-6361/201322068)
- Astropy Collaboration, Price-Whelan, A. M., Sipőcz, B. M., et al. 2018, *AJ*, 156, 123, doi: [10.3847/1538-3881/aabc4f](https://doi.org/10.3847/1538-3881/aabc4f)
- Ballet, J., Burnett, T. H., Digel, S. W., & Lott, B. 2020, arXiv e-prints, arXiv:2005.11208. <https://arxiv.org/abs/2005.11208>
- Blandford, R., Meier, D., & Readhead, A. 2019, *ARA&A*, 57, 467, doi: [10.1146/annurev-astro-081817-051948](https://doi.org/10.1146/annurev-astro-081817-051948)
- Blinov, D., Kiehlmann, S., Pavlidou, V., et al. 2021, *MNRAS*, 501, 3715, doi: [10.1093/mnras/staa3777](https://doi.org/10.1093/mnras/staa3777)
- Boccardi, B., Migliori, G., Grandi, P., et al. 2019, *A&A*, 627, A89, doi: [10.1051/0004-6361/201935183](https://doi.org/10.1051/0004-6361/201935183)
- Caproni, A., Mosquera Cuesta, H. J., & Abraham, Z. 2004, *ApJL*, 616, L99, doi: [10.1086/426863](https://doi.org/10.1086/426863)
- Cara, M., & Lister, M. L. 2008, *ApJ*, 674, 111, doi: [10.1086/525554](https://doi.org/10.1086/525554)
- Chang, Y.-L., Arsioli, B., Giommi, P., & Padovani, P. 2017, *A&A*, 598, A17, doi: [10.1051/0004-6361/201629487](https://doi.org/10.1051/0004-6361/201629487)
- Chang, Y. L., Arsioli, B., Giommi, P., Padovani, P., & Brandt, C. H. 2019, *A&A*, 632, A77, doi: [10.1051/0004-6361/201834526](https://doi.org/10.1051/0004-6361/201834526)
- Cheng, X. P., An, T., Frey, S., et al. 2020, *ApJS*, 247, 57, doi: [10.3847/1538-4365/ab791f](https://doi.org/10.3847/1538-4365/ab791f)
- Davis, S. W., & Tchekhovskoy, A. 2020, *ARA&A*, 58, 407, doi: [10.1146/annurev-astro-081817-051905](https://doi.org/10.1146/annurev-astro-081817-051905)
- Deller, A. T., Brisken, W. F., Phillips, C. J., et al. 2011, *PASP*, 123, 275, doi: [10.1086/658907](https://doi.org/10.1086/658907)
- Dey, L., Valtonen, M. J., Gopakumar, A., et al. 2021, *MNRAS*, 503, 4400, doi: [10.1093/mnras/stab730](https://doi.org/10.1093/mnras/stab730)
- Fabian, A. C. 2012, *ARA&A*, 50, 455, doi: [10.1146/annurev-astro-081811-125521](https://doi.org/10.1146/annurev-astro-081811-125521)
- Falceta-Gonçalves, D., Caproni, A., Abraham, Z., Teixeira, D. M., & de Gouveia Dal Pino, E. M. 2010, *ApJL*, 713, L74, doi: [10.1088/2041-8205/713/1/L74](https://doi.org/10.1088/2041-8205/713/1/L74)
- Fomalont, E. B. 1999, in *Astronomical Society of the Pacific Conference Series*, Vol. 180, *Synthesis Imaging in Radio Astronomy II*, ed. G. B. Taylor, C. L. Carilli, & R. A. Perley, 301
- Gower, A. C., Gregory, P. C., Unruh, W. G., & Hutchings, J. B. 1982, *ApJ*, 262, 478, doi: [10.1086/160442](https://doi.org/10.1086/160442)
- Greisen, E. W. 2003, in *Astrophysics and Space Science Library* 285, *Information Handling in Astronomy – Historical Vistas*, ed. A. Heck (Dordrecht: Kluwer), 109
- Hervet, O., Boisson, C., & Sol, H. 2015, *A&A*, 578, A69, doi: [10.1051/0004-6361/201425330](https://doi.org/10.1051/0004-6361/201425330)
- Homan, D. C., Ojha, R., Wardle, J. F. C., et al. 2002, *ApJ*, 568, 99, doi: [10.1086/338701](https://doi.org/10.1086/338701)
- Homan, D. C., Kovalev, Y. Y., Lister, M. L., et al. 2006, *ApJL*, 642, L115, doi: [10.1086/504715](https://doi.org/10.1086/504715)
- Hovatta, T., Lister, M. L., Aller, M. F., et al. 2012, *AJ*, 144, 105, doi: [10.1088/0004-6256/144/4/105](https://doi.org/10.1088/0004-6256/144/4/105)
- Jones, D. H., Saunders, W., Read, M., & Colless, M. 2005, *PASA*, 22, 277, doi: [10.1071/AS05018](https://doi.org/10.1071/AS05018)
- Jorstad, S. G., Marscher, A. P., Morozova, D. A., et al. 2017, *ApJ*, 846, 98, doi: [10.3847/1538-4357/aa8407](https://doi.org/10.3847/1538-4357/aa8407)
- Kellermann, K. I., Vermeulen, R. C., Zensus, J. A., & Cohen, M. H. 1998, *AJ*, 115, 1295, doi: [10.1086/300308](https://doi.org/10.1086/300308)
- Komatsu, E., Dunkley, J., Nolta, M. R., et al. 2009, *ApJS*, 180, 330, doi: [10.1088/0067-0049/180/2/330](https://doi.org/10.1088/0067-0049/180/2/330)
- Komissarov, S., & Porth, O. 2021, *NewAR*, 92, 101610, doi: [10.1016/j.newar.2021.101610](https://doi.org/10.1016/j.newar.2021.101610)
- Lawrence, C. R., Pearson, T. J., Readhead, A. C. S., & Unwin, S. C. 1986, *AJ*, 91, 494, doi: [10.1086/114027](https://doi.org/10.1086/114027)
- Lister, M. L., Aller, M. F., Aller, H. D., et al. 2018, *ApJS*, 234, 12, doi: [10.3847/1538-4365/aa9c44](https://doi.org/10.3847/1538-4365/aa9c44)
- . 2015, *ApJL*, 810, L9, doi: [10.1088/2041-8205/810/1/L9](https://doi.org/10.1088/2041-8205/810/1/L9)
- Lister, M. L., & Homan, D. C. 2005, *AJ*, 130, 1389, doi: [10.1086/432969](https://doi.org/10.1086/432969)
- Lister, M. L., Homan, D. C., Kovalev, Y. Y., et al. 2020, *ApJ*, 899, 141, doi: [10.3847/1538-4357/aba18d](https://doi.org/10.3847/1538-4357/aba18d)
- Lister, M. L., Aller, H. D., Aller, M. F., et al. 2009a, *AJ*, 137, 3718, doi: [10.1088/0004-6256/137/3/3718](https://doi.org/10.1088/0004-6256/137/3/3718)
- Lister, M. L., Cohen, M. H., Homan, D. C., et al. 2009b, *AJ*, 138, 1874, doi: [10.1088/0004-6256/138/6/1874](https://doi.org/10.1088/0004-6256/138/6/1874)
- Lister, M. L., Aller, M. F., Aller, H. D., et al. 2013, *AJ*, 146, 120, doi: [10.1088/0004-6256/146/5/120](https://doi.org/10.1088/0004-6256/146/5/120)
- . 2016, *AJ*, 152, 12, doi: [10.3847/0004-6256/152/1/12](https://doi.org/10.3847/0004-6256/152/1/12)
- Lister, M. L., Homan, D. C., Hovatta, T., et al. 2019, *ApJ*, 874, 43, doi: [10.3847/1538-4357/ab08ee](https://doi.org/10.3847/1538-4357/ab08ee)
- Liu, S., & Melia, F. 2002, *ApJL*, 573, L23, doi: [10.1086/341991](https://doi.org/10.1086/341991)
- Lomb, N. R. 1976, *Ap&SS*, 39, 447, doi: [10.1007/BF00648343](https://doi.org/10.1007/BF00648343)

- Matveyenko, L. I., & Seleznev, S. V. 2015, *Astronomy Letters*, 41, 712, doi: [10.1134/S1063773715120099](https://doi.org/10.1134/S1063773715120099)
- Meyer, E. T., Fossati, G., Georganopoulos, M., & Lister, M. L. 2011, *ApJ*, 740, 98, doi: [10.1088/0004-637X/740/2/98](https://doi.org/10.1088/0004-637X/740/2/98)
- Nieppola, E., Tornikoski, M., & Valtaoja, E. 2006, *A&A*, 445, 441, doi: [10.1051/0004-6361:20053316](https://doi.org/10.1051/0004-6361:20053316)
- Nieppola, E., Valtaoja, E., Tornikoski, M., Hovatta, T., & Kotiranta, M. 2008, *A&A*, 488, 867, doi: [10.1051/0004-6361:200809716](https://doi.org/10.1051/0004-6361:200809716)
- Nolan, P. L., Abdo, A. A., Ackermann, M., et al. 2012, *ApJS*, 199, 31, doi: [10.1088/0067-0049/199/2/31](https://doi.org/10.1088/0067-0049/199/2/31)
- Ojha, R., Homan, D. C., Roberts, D. H., et al. 2004, *ApJS*, 150, 187, doi: [10.1086/379662](https://doi.org/10.1086/379662)
- Orienti, M., Dallacasa, D., Tinti, S., & Stanghellini, C. 2006, *A&A*, 450, 959, doi: [10.1051/0004-6361:20054656](https://doi.org/10.1051/0004-6361:20054656)
- Piner, B. G., Pant, N., & Edwards, P. G. 2010, *ApJ*, 723, 1150, doi: [10.1088/0004-637X/723/2/1150](https://doi.org/10.1088/0004-637X/723/2/1150)
- Plavin, A. V., Kovalev, Y. Y., Pushkarev, A. B., & Lobanov, A. P. 2019, *MNRAS*, 485, 1822, doi: [10.1093/mnras/stz504](https://doi.org/10.1093/mnras/stz504)
- Pushkarev, A. B., Kovalev, Y. Y., Lister, M. L., & Savolainen, T. 2017, *MNRAS*, 468, 4992, doi: [10.1093/mnras/stx854](https://doi.org/10.1093/mnras/stx854)
- Qian, S.-J., Britzen, S., Witzel, A., et al. 2014, *Research in Astronomy and Astrophysics*, 14, 249, doi: [10.1088/1674-4527/14/3/001](https://doi.org/10.1088/1674-4527/14/3/001)
- Rau, A., Schady, P., Greiner, J., et al. 2012, *A&A*, 538, A26, doi: [10.1051/0004-6361/201118159](https://doi.org/10.1051/0004-6361/201118159)
- Readhead, A. C. S., Ravi, V., Lioudakis, I., et al. 2021, *ApJ*, 907, 61, doi: [10.3847/1538-4357/abd08c](https://doi.org/10.3847/1538-4357/abd08c)
- Richards, J. L., Max-Moerbeck, W., Pavlidou, V., et al. 2011, *ApJS*, 194, 29, doi: [10.1088/0067-0049/194/2/29](https://doi.org/10.1088/0067-0049/194/2/29)
- Roberts, D. H., Wardle, J. F. C., Lipnick, S. L., Selesnick, P. L., & Slutsky, S. 2008, *ApJ*, 676, 584, doi: [10.1086/527544](https://doi.org/10.1086/527544)
- Sargent, W. L. W. 1970, *ApJ*, 160, 405, doi: [10.1086/150443](https://doi.org/10.1086/150443)
- Scargle, J. D. 1982, *ApJ*, 263, 835, doi: [10.1086/160554](https://doi.org/10.1086/160554)
- Schramm, K.-J., Borgeest, U., Kuehl, D., et al. 1994, *A&AS*, 106, 349
- Shaw, M. S., Romani, R. W., Cotter, G., et al. 2012, *ApJ*, 748, 49, doi: [10.1088/0004-637X/748/1/49](https://doi.org/10.1088/0004-637X/748/1/49)
- . 2013, *ApJ*, 764, 135, doi: [10.1088/0004-637X/764/2/135](https://doi.org/10.1088/0004-637X/764/2/135)
- Shepherd, M. C. 1997, in *Astronomical Society of the Pacific Conference Series*, Vol. 125, *Astronomical Data Analysis Software and Systems VI*, ed. G. Hunt & H. E. Payne (San Francisco: ASP), 77
- Smith, M. D., & Donohoe, J. 2019, *MNRAS*, 490, 1363, doi: [10.1093/mnras/stz2525](https://doi.org/10.1093/mnras/stz2525)
- Stephens, M. A. 1974, *Journal of the American Statistical Association*, 69, 730, doi: [10.1080/01621459.1974.10480196](https://doi.org/10.1080/01621459.1974.10480196)
- Stratta, G., Capalbi, M., Giommi, P., et al. 2011, *ArXiv e-prints*, 1103.0749. <https://arxiv.org/abs/1103.0749>
- Thompson, D. J., Djorgovski, S., Vigotti, M., & Grueff, G. 1992, *ApJS*, 81, 1, doi: [10.1086/191683](https://doi.org/10.1086/191683)
- Truebenbach, A. E., & Darling, J. 2017, *ApJS*, 233, 3, doi: [10.3847/1538-4365/aa9026](https://doi.org/10.3847/1538-4365/aa9026)
- Varshalovich, D. A., Levshakov, S. A., Nazarov, E. A., Spiridonova, O. I., & Fomenko, A. F. 1987, *AZh*, 64, 262
- Vermeulen, R. C., Ros, E., Kellermann, K. I., et al. 2003, *A&A*, 401, 113, doi: [10.1051/0004-6361:20021752](https://doi.org/10.1051/0004-6361:20021752)
- Wang, A., An, T., Jaiswal, S., et al. 2021, *MNRAS*, 504, 3823, doi: [10.1093/mnras/stab587](https://doi.org/10.1093/mnras/stab587)
- Wardle, J. F. C. 2013, in *European Physical Journal Web of Conferences*, Vol. 61, *European Physical Journal Web of Conferences*, 06001, doi: [10.1051/epjconf/20136106001](https://doi.org/10.1051/epjconf/20136106001)
- Wardle, J. F. C., & Kronberg, P. P. 1974, *ApJ*, 194, 249, doi: [10.1086/153240](https://doi.org/10.1086/153240)
- Xiong, D., Zhang, X., Bai, J., & Zhang, H. 2015, *MNRAS*, 450, 3568, doi: [10.1093/mnras/stv812](https://doi.org/10.1093/mnras/stv812)